EFFECT OF THE ROTATING DOMAIN SIZE IN MULTIPLE REFERENCE FRAME SIMULATIONS OF TWO RADIAL FLOW IMPELLERS IN A BAFFLED STIRRED TANK

by

Aarón Delfino De La Concha Gómez

A thesis submitted to the School of Graduate Studies
In partial fulfillment of the requirements for the degree of

Doctor en Ingeniería de Procesos

Dr. Jorge Ramírez Muñoz
Director

Dr. Alejandro Rafael Alonso Gómez
Codirector

Universidad Autónoma Metropolitana-Azcapotzalco

June 2019

Azcapotzalco México City

Contents

LIST OF FIGURES

LIST OF TABLES

Nomenclature		Units (SI)
C	Impeller off-bottom clearance	[mm]
$C_{1\varepsilon}$, $C_{2\varepsilon}$, C_{μ}	κ-ε model constants	[--]
D	Impeller diameter	[mm]
F_{cent}	Centrifugal force	[N·m^{-3}]
F_{cor}	Coriolis force	[N·m^{-3}]
Gκ	Generation of κ	
J	Baffle width	[mm]
N	Impeller speed	[s^{-1}]
Np	Power number	[--]
Q	Pumping capacity	[m^3·s^{-1}]
R	Impeller radius	[mm]
$\vec{r}$	location vector	[m]
Re	Reynolds number	[--]
T	Tank diameter	[mm]
H	Baffle height	[mm]

$\vec{u}$	Velocity vector	[m·s^{-1}]
u_i, u_j	Velocity components	[m·s^{-1}]
$\overline{u}_i$	Mean velocity	[m·s^{-1}]
u_i'	Instantaneous velocity	[m·s^{-1}]
W	Blade width	[mm]
x, y, z	Cartesian coordinates	[m]
Z	Liquid height at rest	[mm]
TiO_2	Titanium Dioxide	

Abbreviations

˚Bx	Degrees Brix
BSV	Blades Swept Volume
CFD	Computational Fluid Dynamics
MRF	Multiple Reference Frame
rpm	Revolutions per minute
RRF	Rotating Reference Frame
RRF1 to RRF6	Different rotating reference frame regions
SM	Sliding Mesh
SRF	Static Reference Frame
V1 to V6	Volumes of fluid around the impeller
HSI	High Shear Impeller
N-S	Navier-Stokes equations
RANS	Reynolds Averaged Navier-Stokes
RT	Rushton Turbine
PBT	Pitched-Blade Turbine
RNG	Re-Normalization Group
RSM	Reynolds Stress Turbulence Model
SST	SST Shear Stress Turbulence
DNS	Direct Numerical Simulation
FVM	Finite Volume Method

Greek letters

ρ	Density	[kg · m^{-3}]
$\Im$	Torque	[N·m]
μ	Viscosity	[Pa · s]
μ_t	Turbulent viscosity	[Pa · s]
ε	Turbulent energy dissipation rate	[m^2·s^{-3}]
κ	Turbulent kinetic energy	[m^2·s^{-2}]
σ_κ, σ_ε	κ-ε model constants	[--]
ω	Angular velocity	[s^{-1}]

ABSTRACT

A computational fluid dynamics (CFD) study was conducted in order to simulate the flow induced by both a turbine of four flat blades, and a high shear impeller (HSI) Norstone® type. The investigation was carried out in a stirred baffled-tank operating in laminar and turbulent flow conditions. To account for the rotation of the impeller-shaft array, the multiple reference frame (MRF) approach is employed, which in its core demands a demarcation for a surface separating the computational domain into two very distinctive regions: the rotating reference frame (RRF) and the static reference frame (SRF).

This research project focuses specifically on investigating the role of the location of the separating surface over the accuracy of numerical approximations. To this end, several cylindrical volumes are constructed surrounding each of the impellers. In order to conduct simulations of the stirred-tank working at Reynolds numbers below 115, the laminar model was considered, whereas for Reynolds numbers above 21000, the standard κ-ε turbulence model was employed. To validate the digital replicas employed in the numerical simulations, power number measurements corresponding to laminar and turbulent flow regimes were obtained from a lab-scale cylindrical stirred-tank equipped with either of the two impellers previously mentioned.

The computer results reveal that in the case of laminar flow, the position of the surface separating both regions for the two evaluated impellers do not have a substantial effect on the corresponding numerical approximations. However, its position influences numerical accuracy as the Reynolds number increases, i.e., the higher this is, the larger the RRF must be. The optimal extension for the RRF-region for the four flat blades impeller found in this work in turbulent flow were employed for reproducing satisfactorily experimental results of a published system.

An analysis based on grid density for the two digital replicas built for this study, revealed that numerical power number values and local velocity profiles are more sensitive to changes in the extension of the RRF domain rather than to an increase in the number of grid points for the mesh representing the stirred-tank system equipped with the four flat-blade turbine. On the other hand, in the case of the stirred-tank system equipped with the Norstone® impeller, sensitive changes were only substantial in the case of the velocity profiles.

1 INTRODUCTION

Important industries like mineral processing, pharmaceuticals, petrochemicals, food, drinking water and wastewater management among many others, rely heavily on the employment of mixing equipment. By mixing, we can understand the reduction of inhomogeneity in order to achieve a desired process result. The inhomogeneity can be one of concentration, phase, or temperature. Secondary effects, such as mass transfer, reaction and product properties are usually the critical objectives (Paul et al., 2004).

Mixing operations are regularly conducted employing stirred-tanks, which are characterized by two particular properties. One of these can be attributed to the form of the tank itself, commonly possessing a cylinder-like shape with its bottom-end being either flat or rounded. The other characteristic stands for the way in which energy is injected to the working fluid confined in the tank. To this end, a mixer (impeller) directly attached to a vertical shaft, is set to spin generating in the impeller kinetic energy which is immediately transferred to the fluid by the contact existing between the surfaces of the impeller and the adjacent layer of the fluid.

Choosing the right mixer for an application depends on the process requirements (Dickey et al., 2004), for instance, industries interested in enhancing gas-liquid or liquid-liquid dispersion processes, might benefit from employing impellers such as the four flat blades turbine capable to induce radial flow. With suitable baffles these flows are converted to strong top-to-bottom flows both above and below the impeller. These kind of impellers are known to provide high shear and turbulence levels with lower pumping (Paul et al., 2004). In the coating industry, it is well-known that an optimal dispersion maximizes the hiding power and minimizes the amount of pigments used for a specific formulation (Ramírez-Gómez et al., 2015). Pigment nanoparticles, such as TiO_2, aggregate very easily during storage owing to their large specific surface area. Therefore, it is extremely important to obtain uniform dispersion of pigment particles to achieve the quality specifications of the final product (Martínez-de Jesús et al., 2017). To this end, a specialized mixer device known as high shear impellers (HSIs) such as the Norstone® impeller operating at relatively high velocities in the laminar to transitional flow regime is employed to break particle

agglomerates and disperse them in liquids until a certain desired degree of homogeneity is attained (Martínez-de Jesús et al., 2017).

Mixing operations can be conducted at constant impeller speeds on which the stirred fluid might change its viscosity (exceeding four orders of magnitude) during the different stages of its manufacturing processes, e.g., xanthan gum fermentation (Galindo et al., 1992) and homogenization of water-based paints (Patton, 1979), thus excluding the possibility of removing the baffles out of the vessel. Although, it is a common practice to deal fluid mixing in the laminar to transitional flow regime without the usage of baffles (Ramírez-Gómez et al., 2015; Zalc et al., 2001), it is possible to find baffled-tanks operating at low Reynolds numbers corresponding to laminar creeping flow (Kelly et al., 2003; Pakzad et al., 2013).

Significant improvements on the design, capability and reliability of stirred reactors may be expected from advances in computational fluid dynamics (CFD) simulation techniques. CFD simulations offer the only cost-effective means to acquire the detailed information on flow and turbulence fields needed for realistic distributed-parameter process simulations. Moreover, with CFD-based simulations the actual size of the process equipment can be effectively dealt with, so that scale-up uncertainties are avoided (Montante et al., 2001).

When conducting CFD-oriented studies in stirred tanks, a fundamental feature to account for is the modeling of the impeller motion. In the pursue of this aspect, various approaches have been considered, among these, the most commonly employed are the sliding-grid approach also known as the Sliding-Mesh (SM), first introduced by Luo (1993), and the Multiple Reference Frame (MRF) introduced by Luo et al. (1994) (Brucato et al., 1998; Deen et al., 2002; Fathi Roudsari et al., 2012; Lane et al., 2000; B. N. Murthy et al., 2008).

In the SM approach, the computational domain representing the stirred-tank system has to be divided into two distinctive separated regions. The first of these regions is a cylinder-like region which is located inside the system immediately surrounding the impeller. The other region which comprises the remainder of the computational domain is located right after the first one. An important characteristic for the first region, is that this is set to spin at the same

angular velocity of the impeller-shaft, for this reason, at the interface between the two parts the mesh is allowed to shear and/or slide to accommodate the relative motions (Luo, 1993).

The SM approach conducts transient-state numerical approximations for successive time steps accounting for the relative position of the impeller and the baffles. SM has been recognized for its capability to yield fully predictive simulations (Montante et al., 2001). This method is appropriate for analysis of unsteady operations such as initial start-up of agitation systems and for modeling with entire accuracy the impeller-baffle interaction, however, its computational cost is very high.

On the other hand, for most current applications of interest, it has been stablished that the interaction between impeller and the baffles is somehow weak. This weakness has been proposed for dimensionless geometric ratios up to $D/T \approx 0.5$ (Oshinowo et al., 2000), where D and T are the impeller and the tank inner diameter, respectively. The previous proposal means that a cyclical unsteady flow field will appear after a certain number of impeller rotations, meaning that the relative position of the impeller with respect to the baffles is now not essential at all, thus steady-state simulations now considering the MRF approach can be conducted.

The MRF methodology resembles the SM approach in the sense that it demands a compulsory splitting of the computational domain into two clearly distinctive regions. Here too a cylinder-like region known as the Rotative Reference Frame (RRF) is positioned to be directly attached to the impeller. Within this bounded region, the reference frame is set to spin at the same impeller angular velocity promoting that the conservation equations then have to be subjected to a transformation process which gives rise to two additional terms (i.e., the centrifugal and Coriolis force) located in the momentum equations. The other region also considered in this approach is the Static Reference Frame (SRF) region, which comprises the remainder of the computational domain, on which a laboratory (or static) reference frame is used (Luo et al., 1994). When conducting MRF-oriented studies, the numerical approximations computed within the RRF domain have to be transferred outwardly to the SRF domain by means of boundary conditions for all flow properties at the interface, and an

iterative approach between both regions is required to achieve a converged solution (Sommerfeld et al., 2004).

Compared to the computational requirements demanded by the SM approach, the MRF methodology is much more computationally efficient, for the reason that this takes advantage of conducting steady-state calculations, this result in that its computational requirements are around one order of magnitude lower (Brucato et al., 1998; Lane et al., 2000; Wechsler et al., 1999). Furthermore, it has been reported that the numerical results both yields are comparable (Brucato et al., 1998; Wechsler et al., 1999).

As a consequence, the MRF methodology has been largely employed in CFD simulations of stirred tanks operating at various flow regimes (Ameur et al., 2012; Ammar et al., 2012; Chtourou et al., 2014; Deglon et al., 2006; Devi et al., 2015; Ein-Mozaffari et al., 2009; Glover et al., 2007; Joshi et al., 2011a, 2011b; Pakzad et al., 2008; Rahimi et al., 2010; Ramírez-Gómez et al., 2015; Ramírez-Muñoz et al., 2016; Sossa-Echeverria et al., 2012; Tabor et al., 1996), but when it comes to considering CFD-oriented studies focused exclusively on stirred baffled-tanks operating in turbulent conditions, it has been pointed out that the location for the surface separating the RRF and SRF regions is by no means arbitrary. It has been pointed out that this has to be properly placed where flow variables do not change appreciably either through the azimuthal direction or with time, i.e., when an almost steady flow is established at this position (Joshi et al., 2011a; Sommerfeld et al., 2004).

In the search for recommendations specifying exactly where to properly place this cylinder-like surface separating the RRF region from the SRF region, a thorough review in the literature specialized in the subject revealed that only few research works have been directed to investigate this issue. Moreover, it was found that no consensus exists between these works consulted.

As a consequence, this research work emerges as an attempt to answer this important question regarding the location of this separating surface, specifically, to investigate if the flow regime under consideration plays and important role in the extension of this surface which in turn might impact in the reliability of the numerical results computed when employing this modelling approach. In order to conduct this investigation, this research work was divided into chapters each dealing with a specific subject. On chapter 2, the Background, is devoted mainly to provide a review of the most relevant studies conducted so far on which a clear and well define methodology was employed in order to define an extent of the RRF region. Chapter 3 deals with a detailed explanation of the statistical transformation to which the N-S equations were subjected. This chapter also deals in part with the mathematical theory behind the numerical method employed in the simulations known as finite volume, which is a direct result of a classic theorem of calculus known as the Gauss theorem. Although the body of knowledge in this subject is large, the author will make an attempt to explain this as clear as possible for future readers by gathering most of the information needed to this end, but directing to alternative sources if considered otherwise. Since the foundations of this research project resides in the Multi Reference Frame (MRF) approach, the proposal for investigating the influence of the flow regime on the extension of the region enveloping the impeller is explained here. On chapter 4 the results of this project are outlined and presented. Finally, on chapter 5 the conclusions based on the results are drawn, followed by directions which are believed can improve future studies.

2 BACKGROUND

2.1 Literature Review.

When looking for recommendations specifying where to properly place the surface separating the RRF region from the SRF region when the MRF approach is employed, it was found that the Rushton Turbine (RT) has been habitually employed in CFD-oriented studies. For instance, Oshinowo et al. (2000) conducted both experiments and numerical simulations of a baffled-tank agitated by either the RT or a pitched-blade turbine (PBT) working in the turbulent regime. In this work, the authors declare that the optimal location for the radial position of the surface separating the RRF and SRF region should be located roughly midway between the impeller blade tip and the inner radius of the baffles. These authors utilized the κ-ε, RNG κ-ε and RSM models to account for turbulence phenomena. With the previous models, they conducted an analysis to investigate the effects of varying the axial extension of the RRF region in the numerical computations of the flow field, and as a result, they report that there is an influence of this position over the tangential velocity distribution. In their work, the MRF surface was set to ±R above and below the impeller for the radial flow RT, while for the axial flow PBT, the MRF interface was set from ~R to ~4R, where R is the impeller radius.

Other CFD-oriented studies focused on baffled-tanks equipped with a Rushton turbine on which the authors have clearly defined the extension of the RRF domain are the works of Lane et al. (2000), Deglon et al. (2006), Zadravec et al. (2007).

Lane et al. (2000) positioned the interface separating both domains at an axial distance of ±0.5R above and below the impeller centerline, and radially, it was positioned at a distance of 1.5R. Deglon et al. (2006), based their investigation on the experimental data published by K. C. Lee et al. (1994) and they decided that the extent of the RRF in the radial direction should be situated at a distance of half the impeller radius away from the impeller tip, and 1.5 blade widths above and below the impeller edge.

Zadravec et al. (2007) were too motivated on finding a proper location for the surface separating the RRF and SRF domain. In their investigation, they executed numerical simulations complemented with data readings coming out of a particle image velocimetry (PIV) equipment. In their investigation, in order to account for varying the RRF region, they assembled four different cylindrical volumes surrounding the Rushton turbine by varying the radial (~1.11R-1.43R), and axial dimensions (~0.31R-0.64R) above and below the impeller centerline. In order to model turbulent effects, they employed the k-omega shear stress turbulence (SST) model in the simulations. They mentioned that, in order to obtain reliable numerical approximations of the flow field, the RRF region must be sufficiently large as to include the point lying in the radial coordinate where the fluid motion shifts from accelerating into decelerating. They conclude that the best extension for the cylindrical region extending up to 1.43R in the radial direction, and 0.64R in the axial direction above and below the impeller centerline will be the most recommended.

Based on the study conducted by Armenante et al. (1997), Karimi et al. (2012) conducted their investigation testing several turbulence models, among these the standard κ-ε. To account for computer effort savings, only a 45^{O} degree section of the whole tank was considered. The type of impeller employed was a six-blade impeller spinning at a peripheral velocity of 450 rpm. To account for the impeller motion within this unbaffled-stirred tank, these authors employed the MRF approach, resulting in the splitting of the entire vessel into the bulk flow region and the rotational zone, however in this work no specific dimension were provided as to how large the RRF region is.

Karimi (2014), directed a new study considering the same arrangement employed in 2012. In his work, the author conducted numerical simulations in order to find the appropriate extension of the RRF region enveloping the six-blade impeller in order to predict velocity components and turbulent properties (Karimi, 2014). To this end, four different RRF dimensions were allocated at 1, 2, 5, and 7 mm distance from all sides of the blades (i.e., four cylinders with height and length of 16×100 mm, 18×102 mm, 24×108 mm, and 28×112 mm). This author reported that the quantitative comparison of the CFD results with measurements from Armenante et al. (1997) reveals that for the larger rotational zones (i.e., 5 and 7 mm)

the predicted maximum axial velocities have been underpredicted with more than 50% error. In turn, numerical simulations considering the smaller extents of the rotation zones (i.e., 1 and 2 mm), not only captured the location of maximum axial velocity correctly but also they quantitatively match the experiments reasonably well (to within average differences of 16.10% and 7.98% for the 2 mm and 1 mm rotational zones, respectively) (Karimi, 2014). By comparing the numerical predictions of the other velocity components as well as the turbulent kinetic energy and its dissipation rate, Karimi (2014) concluded that the smaller rotational zones (1 mm distance from all sides of the blade) around the impeller enhance the precision of the CFD data. This result was later employed within this same research work to simulate the rotation of a Rushton turbine. Although it might seem that Karimi (2014) reached a conclusion defining were to locate the surface separating the RRF and SRF domains, it is important to mentioned that this author achieved this conclusion by comparing numerical results corresponding to a six-blade radial flow impeller with experimental data related to a six-blade, 45° pitched-blade turbine (Armenante et al., 1997).

Recently, Patil et al. (2018) conducted numerical simulations of a fully baffled-stirred tank agitated by the RT operating in turbulent conditions. The stirred tank configuration employed by these authors, was the same reported by Wu et al. (1989). Patil et al. (2018) proposed a methodology aimed to provide with the optimal extension for the RRF region. To this end, these authors defined seven concentric cylindrical regions enveloping this radial flow impeller to account for progressively varying the extension of the RRF region within the numerical simulations. In addition to the MRF approach employed here, they selected the realizable k-ε model to account for turbulent effects. Based on their analysis, these authors conclude that in order to obtain a good match between flow parameters extracted from CFD simulations and experimental results, the cylindrical zone extending radially to twice the impeller radius (2R), and in the axial direction up to 0.62R above and below the impeller centerline, should be considered as the optimal for CFD modeling of the stirred-tank. With this selection, these authors enabled accurate predictions of the power number (N_P) covering from laminar up to turbulent flow conditions.

Although Zadravec et al. (2007) and Patil et al. (2018) conducted studies applying a straightforward and well-defined methodology considering a similar stirred-tank system, it

turns out that the results these authors obtained are by all means different. Moreover, across the entirety of the works consulted, it was noticed that all methodologies followed were developed considering exclusively Re covering the turbulent flow regime, leaving out of the scope the laminar flow regime and its probable influence over the location of the separating surface. In addition, to the best of the author's knowledge, the Rushton turbine is not commonly employed to conduct mixing in large industrial stirred-tanks, so relevant results that might be obtained based on this impeller, will likely to have limited impact in industrial applications.

2.2 Justification

As was mentioned above, no consensus exists in the literature as to where the extension of the RRF region must be defined when conducting CFD simulations of stirred-tanks employing the MRF approach. As a consequence, this CFD-oriented research work emerges as an attempt to answer this important question by considering stirred-tanks agitated by the four flat-blade turbine and the Norstone© impeller. In addition, this research work expands the analysis by investigating the impact it has on the extension of the RRF region an extra variable such as the Re number (i.e., the flow regime at which the stirred-tank is conducting mixing operations: laminar and turbulent). To address the previous concerns, this research work is grounded on the following steps:

2.3 Hypotheses

The starting point for this research work is provided by the next hypotheses:

- The employment of two different radial flow impellers in CFD simulations of a stirred-tank might result in different extensions for the RRF region.
- The flow regime under consideration (laminar or turbulent) might promote an increase in the extension of the RRF region, which in turn might impact in the reliability of the numerical approximations.

2.4 Objectives

2.4.1 General

To investigate the effect of the rotating domain extension within numerical multiple reference frame simulations of two radial flow impellers in a baffled stirred-tank.

2.4.2 Particular

- To assemble around in each of the digital replicas accounting for the two impellers employed (i.e., four flat-blade turbine and Norstone® impeller), several cylindrical volumes to account for modifying the extension of the RRF region within the numerical simulations.
- To gather power number readings covering the laminar and turbulent regimes from lab-scale stirred baffled-tanks in order to validate numerical simulations.
- To study the response of some important hydrodynamical parameters (power number, velocity magnitude, shear rate) as a function of the RRF size for both impellers considered in laminar and turbulent flow regimes.
- To find the RRF size where the numerical results are independent of its dimension as well as the flow regimes (i.e., the laminar and turbulent).

3 EXPERIMENTAL AND NUMERICAL METHODOLOGY

3.1 Experimental Methodology.

Laboratory-scale experiments were conducted in order to collect data representing power number measurements for the stirred-tank system being agitated with each of the two impellers considered in this research work. This collected data was later employed to validate the accuracy of the digital replicas (see section 4.1). The experimental equipment employed at the lab-scale consisted of a jacketed stainless-steel dish-bottomed cylindrical tank with an inner diameter T=132 mm, assembled with four equally-spaced baffles of height H=110 mm, width J=13.2 mm, and thickness of 1 mm, thus J/T=1/10. The separation between the tank wall and the baffles was set at a distance of 5.72 mm. Ratios C/T and D/T, for which C represents the bottom off clearance measured from the impeller midplane, resulted in 0.3848. Height (Z) which corresponds to the liquid interface remaining at rest was equal to T, thus, Z/T=1, D/W was set to 5, where W is the corresponding impeller width. All previous considerations resulted in a fluid volume of 1.63 L for the stirred-tank system equipped with the four flat-blade turbine, and 1.62 L for the stirred-tank system equipped with the Norstone® impeller. The dimensions for the two custom-made polylactic acid 3D-printed impellers can be consulted in Figure 3.1 Impellers employed in this research work..

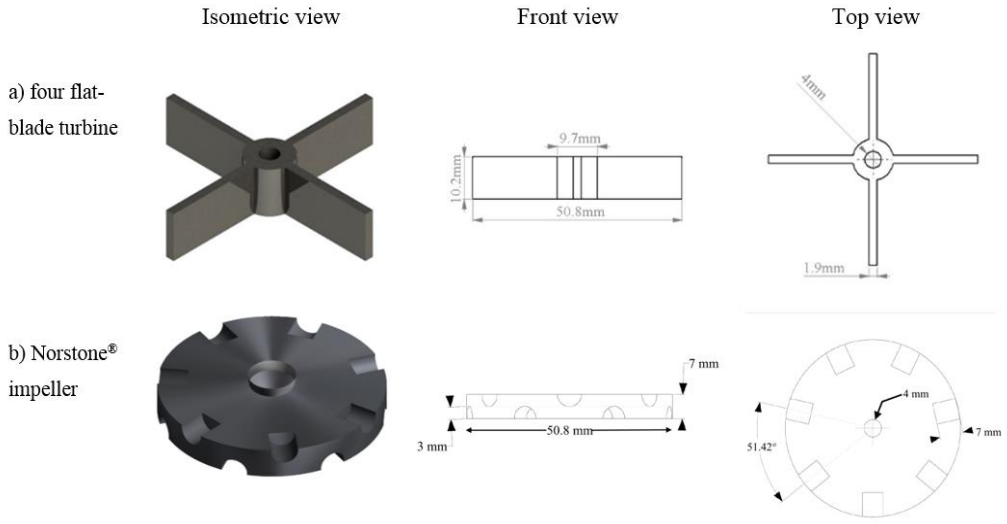

Figure 3.1 Impellers employed in this research work.

Mechanical agitation for either of the two impellers was provided by a user-controlled speed Dispermat® AE01 device (VMA-Getzmann GmbH, Germany), with 0.75 HP nominal power, inducing in the impeller-shaft array rotation in the clockwise direction. To maintain a constant fluid temperature of 23.0±0.5°C during all experimental runs, cooling (or warming) water was recirculated through the vessel jacket. Torque readings were obtained employing a Futek® TRH300-FSH1980 (Futek Advanced Sensor Technology, USA) data acquisition system directly attached to the shaft. This transducer has a maximum capacity of 6 N·m, a resolution of 6 mN·m and a full-scale precision of 0.5%. Previously, it has been reported that this equipment can reproduce adequately power number values reported by Rushton et al. (1953) for a Rushton turbine operating in the laminar flow regime (Ramírez-Muñoz et al., 2017). Figure 3.2. Experimental setup shows a diagram of the equipment employed

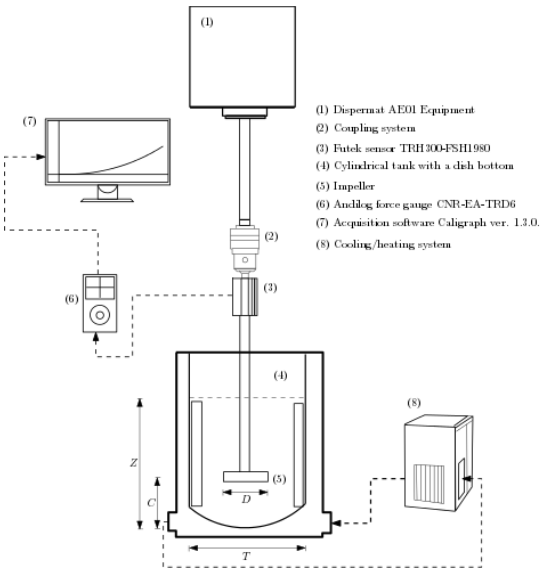

Figure 3.2. Experimental setup

To account for the intervals containing the Reynolds numbers considered in this research work ($1 \leq Re < 116$ and $21473 \geq Re \geq 42946$), four different Newtonian fluids were use as working fluids in these lab-scale experiments. These consisted of three solutions prepared from a 45 °Bx food grade glucose and distilled water at mass glucose concentrations of 37.5% (fluid 1), 36.32% (fluid 2), 32.21% (fluid 3) and 0% (i.e., distilled water, fluid 4), respectively. For fluids 1-3, viscosity values were gathered from rotational measurements at

23˚C using an Anton Paar MCR 502 rheometer with concentric cylinder geometry, whilst their respective densities were measured by using a graduated cylinder and an analytical balance. Data for pure distilled water were obtained from Perry et al. (2008). Table 3.1 Fluids considered in this study.shows the density (ρ) and viscosity (μ) properties of the four employed fluids, the impeller rotational speed (N), as well as the impeller Reynolds number ($Re= \rho ND2/\mu$) covered for the experimental power draw validations for each fluid.

Table 3.1 Fluids considered in this study.

Fluid	ρ(kg·m^{-3})	μ(Pa-s)	N interval (rpm)	Reynolds covered	
1	1365	2.4	40 - 1200	1 - 29.4,	laminar
2	1338	1.082	300 - 1500	16 - 79.8,	laminar
3	1317.4	0.4889	400 - 1000	46.4 – 115.9,	laminar
4	998.5	0.001	500 - 1000	21473 – 42946,	turbulent

The data stream coming out of the Futek® consisting in torque measurements registered over a time span of 60 seconds, was gathered and processed in order to compute mean values of the torque induced by each of the two impellers at the selected impeller rotational speeds. A typical torque signal obtained with the Futek® is showed in Figure 3.3

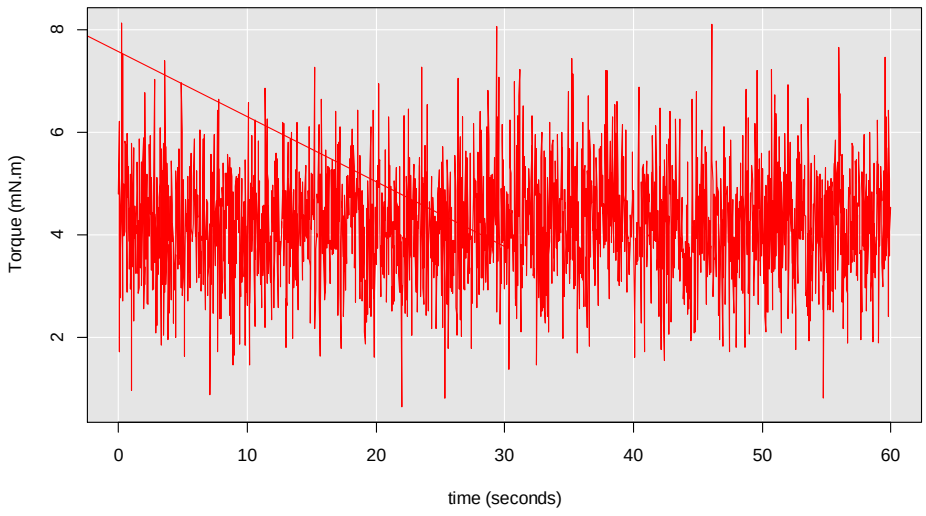

Figure 3.3 Torque signal obtained from the Futek® transducer.

All mean torque values were then organized in a straightforward manner in order to compute power number (N_P) curves covering laminar and turbulent flow for the two impellers. By

analyzing resemblance between these experimentally assembled curves and numerically assembled curves, then a final decision can be made with regards to the validity of both computer models in order to be used as a reliable computer-based prediction tools for stirred-tank systems. These power curves, the consecutive analysis and a more robust analysis with regards to the influence of the RRF region on numerical simulations are explained in chapter 4.

3.2 Numerical Methodology.

3.2.1 Navier-Stokes Equations.

Motion in all its forms (i.e., laminar, transitional and turbulent) for incompressible (i.e., ρ constant) Newtonian fluids (i.e., μ constant) can be described by the set of second order non-linear Partial Differential Equations (PDEs) known as Navier-Stokes (N-S):

$$\frac{\partial u}{\partial x}+\frac{\partial v}{\partial y}+\frac{\partial w}{\partial z}=0, \tag{1}$$

$$\left[\frac{Du}{Dt}\right]=-\frac{1}{\rho}\frac{\partial p}{\partial x}+\nu\left[\frac{\partial^2 u}{\partial x^2}+\frac{\partial^2 u}{\partial y^2}+\frac{\partial^2 u}{\partial z^2}\right]+g_x, \tag{2}$$

$$\left[\frac{Dv}{Dt}\right]=-\frac{1}{\rho}\frac{\partial p}{\partial y}+\nu\left[\frac{\partial^2 v}{\partial x^2}+\frac{\partial^2 v}{\partial y^2}+\frac{\partial^2 v}{\partial z^2}\right]+g_y, \tag{3}$$

$$\left[\frac{Dw}{Dt}\right]=-\frac{1}{\rho}\frac{\partial p}{\partial z}+\nu\left[\frac{\partial^2 w}{\partial x^2}+\frac{\partial^2 w}{\partial y^2}+\frac{\partial^2 w}{\partial z^2}\right]+g_z, \tag{4}$$

where u, v and w, are the components of the velocity vector $\vec{u}$ (i.e., $\vec{u}=(u,v,w)$). Ideally, equations (1)-(4) should be solved directly regardless of the flow regime under consideration, which would lead to a DNS modelling (Tamburini et al., 2018). There is no doubt that DNS is the most accurate numerical method due to its capability to solve all length scales (Joshi et al., 2009). A concise list highlighting the important benefits of employing DNS can be outlined based for instance on the book of Versteeg et al. (2007), and the works of Eggels et

al. (1994), Schlatter et al. (2010), and M. Lee et al. (2015); among which perhaps, the most important feature is the ability of DNS to provide results which are in good correspondence with experimental data. However, while most researchers agree that the basic physics of turbulence can be described by the N-S equations (Speziale, 1991), DNS-based studies have the serious disadvantage of being highly costly in terms of the computing effort needed due to the instantaneous range of scales in turbulent flows which increases rapidly with the Reynolds number (~Re^3) (Dijkstra, 2014; Joshi et al., 2011b). As a result, most engineering problems, have too wide a range of scales to be directly computed using DNS, discarding this method to be employed for industrial flow computations (Versteeg et al., 2007).

3.2.2 Statistical decomposition.

On most of the engineering problems dealing with turbulence, the statistical evolution of the flow represented in eqns. (1)-(4) is then considered (Joshi et al., 2011b). To explain this statistical evolution, let us mention that randomness affecting a scalar quantity φ provides a very convenient way to describe this in terms of a combination between a constant mean value (φ) and an instantaneous variation ($\varphi'(t)$) as follows:

$$\varphi(t) = \varphi + \varphi'(t). \tag{5}$$

The core of Reynolds statistical decomposition lies in the application of equation (5), after which a linear operator $E[\cdot]$ can be employed to compute the expected value (assemble average) according to:

$$E[\cdot] = \lim_{t_f \to \infty} \frac{1}{T} \int_{t_0}^{t_f} [\cdot] dt, \tag{6}$$

for a scalar $\varphi(t)$ as follows:

$$E[\varphi(t)] = \lim_{t_f \to \infty} \frac{1}{T} \int_{t_0}^{t_f} [\varphi + \varphi'(t)] dt,$$

$$E[\varphi(t)] = \underbrace{\lim_{t_f \to \infty} \frac{1}{T} \int_{t_0}^{t_f} [\varphi] dt}_{\varphi} + \underbrace{\lim_{t_f \to \infty} \frac{1}{T} \int_{t_0}^{t_f} [\varphi'(t)] dt}_{0},$$

$$E[\varphi(t)] = \varphi. \tag{7}$$

3.2.3 Reynolds Average Navier-Stokes (RANS) Equations.

It can be proved that when applying equations (5) and (7) over equations (1)-(4), this will yield the set of PDEs known as Reynolds Averaged Navier-Stokes (RANS) (Pope, 2000; Versteeg et al., 2007):

$$\frac{\partial u}{\partial x} + \frac{\partial \hat{v}}{\partial y} + \frac{\partial w}{\partial z} = 0, \tag{8}$$

$$\left[\frac{Du}{Dt}\right] = -\frac{1}{\rho}\frac{\partial p}{\partial x} + \nu\left[\frac{\partial^2 u}{\partial x^2} + \frac{\partial^2 u}{\partial y^2} + \frac{\partial^2 u}{\partial z^2}\right] - \frac{1}{\rho}\left[\frac{\partial(\overline{u'u'})}{\partial x} + \frac{\partial(\overline{v'u'})}{\partial y} + \frac{\partial(\overline{w'u'})}{\partial z}\right] + g_x, \tag{9}$$

$$\left[\frac{D\hat{v}}{Dt}\right] = -\frac{1}{\rho}\frac{\partial p}{\partial y} + \nu\left[\frac{\partial^2 \hat{v}}{\partial x^2} + \frac{\partial^2 \hat{v}}{\partial y^2} + \frac{\partial^2 \hat{v}}{\partial z^2}\right] - \frac{1}{\rho}\left[\frac{\partial(\overline{u'v'})}{\partial x} + \frac{\partial(\overline{v'v'})}{\partial y} + \frac{\partial(\overline{w'v'})}{\partial z}\right] + g_y, \tag{10}$$

$$\left[\frac{Dw}{Dt}\right] = -\frac{1}{\rho}\frac{\partial p}{\partial z} + \nu\left[\frac{\partial^2 w}{\partial x^2} + \frac{\partial^2 w}{\partial y^2} + \frac{\partial^2 w}{\partial z^2}\right] - \frac{1}{\rho}\left[\frac{\partial(\overline{u'w'})}{\partial x} + \frac{\partial(\overline{v'w'})}{\partial y} + \frac{\partial(\overline{w'w'})}{\partial z}\right] + g_z. \tag{11}$$

3.2.4 The κ-ε turbulence model.

The transformation of equations (1)-(4) into equations (8)-(11) have brought up new terms to the analysis. The quantities $\overline{v'u'} = \overline{u'v'}$, $\overline{w'u'} = \overline{u'w'}$, $\overline{w'v'} = \overline{v'w'}$, $\overline{u'u'}$, $\overline{v'v'}$, $\overline{w'w'}$ are known as Reynolds stresses. These quantities can be approximated by means of the Boussinesq hypothesis (Boussinesq, 1877) according to:

$$-\rho\overline{u'u'} = 2\mu_t\left[\frac{\partial u}{\partial x}\right] - \frac{2}{3}\rho k, \tag{12}$$

$$-\rho\overline{v'v'} = 2\mu_t\left[\frac{\partial\hat{v}}{\partial y}\right] - \frac{2}{3}\rho k, \tag{13}$$

$$-\rho\overline{w'w'} = 2\mu_t\left[\frac{\partial w}{\partial z}\right] - \frac{2}{3}\rho k, \tag{14}$$

$$-\rho\overline{v'u'} = -\rho\overline{u'v'} = \mu_t\left[\frac{\partial u}{\partial y} + \frac{\partial\hat{v}}{\partial x}\right], \tag{15}$$

$$-\rho\overline{w'u'} = -\rho\overline{u'w'} = \mu_t\left[\frac{\partial u}{\partial z} + \frac{\partial w}{\partial x}\right], \tag{16}$$

$$-\rho\overline{w'v'} = -\rho\overline{v'w'} = \mu_t\left[\frac{\partial w}{\partial y} + \frac{\partial\hat{v}}{\partial z}\right]. \tag{17}$$

The previous approximations have yielded new terms, the turbulent viscosity μ_t and the turbulent kinetic energy k that have to be computed somehow. To this end, several turbulence models exist accounting for approximating μ_t and k (Joshi et al., 2011b; Versteeg et al., 2007). However, since the objective of the present work is not to evaluate the performance of such models, in the context of this research project (agitated-vessels), it is common practice to compute μ_t employing the κ-ε turbulence model (Launder et al., 1974) which is the most established turbulence model for engineering flows and has been widely used for modelling turbulent flow in stirred tanks (Deglon et al., 2006). According to Launder et al. (1974), the turbulent viscosity μ_t can be computed as:

$$\mu_t = \rho C_\mu \frac{\kappa}{\varepsilon}, \tag{18}$$

where the turbulent kinetic energy k, and the rate of dissipation of turbulent kinetic energy ε for this study case (incompressible flow and isothermal conditions) are given by (Fluent, 2015)

$$\frac{\partial(\rho\kappa)}{\partial t}+\frac{\partial(\rho\kappa u_i)}{\partial x_i}=\frac{\partial}{\partial x_j}\left[\left(\mu+\frac{\mu_t}{\sigma_\kappa}\right)\frac{\partial\kappa}{\partial x_j}\right]+G_k-\rho\varepsilon, \tag{19}$$

$$\frac{\partial(\rho\varepsilon)}{\partial t}+\frac{\partial(\rho\varepsilon u_i)}{\partial x_i}=\frac{\partial}{\partial x_j}\left[\left(\mu+\frac{\mu_t}{\sigma_\varepsilon}\right)\frac{\partial\varepsilon}{\partial x_j}\right]+C_{1\varepsilon}\frac{\varepsilon}{\kappa}(G_\kappa)-C_{2\varepsilon}\rho\frac{\varepsilon^2}{\kappa}. \tag{20}$$

The reader interested in the process leading to obtain the previous set of partial differential equations is referred to the book of Versteeg et al. (2007), although a much more detailed and extensive analysis towards the derivation of the previous equations can be found in the work of Scott-Pomerantz (2005).

In equations (19) and (20), G_k represents the generation of turbulence kinetic energy due to the mean velocity gradients. The standard model constants $C_{1\varepsilon}=1.44$, $C_{2\varepsilon}=1.92$, $C_\mu=0.09$, $\sigma_\kappa=1.0$ and $\sigma_\varepsilon=1.3$ have been determined from experiments for fundamental turbulent flows including frequently encountered shear flows like boundary layers, mixing layers and jets as well as for decaying isotropic grid turbulence. They have been found to work fairly well for a wide range of wall-bounded and free shear flows (Fluent, 2015; Joshi et al., 2011b).

On previous works (Abujelala et al., 1984; Armenante et al., 1997; Jenne et al., 1999), it was questioned the capability of the κ-ε model to accurately predict flow properties such as turbulence, however, this was later refuted in the work of Deglon et al. (2006), on which it is demonstrated that when conducting CFD simulations of stirred-tanks using the κ-ε turbulence model within the MRF approach, accurate predictions of the turbulent fluid flow can be obtained, provided that a very fine grids coupled with a higher-order discretization scheme is employed (Deglon et al., 2006). These important findings reported by these authors, provides a very convenient and affordable way to conduct simulations by alleviating significantly the computing effort needed to simulate stirred-vessels working at high Re numbers. From this, it was decided that the findings reported by Deglon et al. (2006) will

constitute the foundations upon which the present work is developed, namely: a) employment of the standard k-epsilon turbulence model with standard model constants, b) the high order QUICK discretization scheme, c) the standard wall functions, and d) the standard pressure-velocity scheme.

3.2.5 The Multiple Reference Frame (MRF) approach.

Previously, it was mentioned that the core of the MRF approach rests in the assumption of weak interaction between the impeller's outer edge (diameter D) and the baffles. If the condition D/T≤0.5 is fulfilled, then this assumption can be taken, which can be depicted as a steady flow field cyclically appearing after a certain number of impeller rotations, this means that the relative position of the impeller with respect to any of the baffles is not essential, thus steady-state simulations as allowed by the MRF approach can be employed. An immediate result of this approach is that all derivatives with respect to time are equal to zero, this fact can be translated into a simpler form for equations (1)-(4) and equations (8)-(11):

$$\vec{u}\cdot\vec{\nabla}(u) = -\frac{1}{\rho}\frac{\partial p}{\partial x} + \nu\left[\frac{\partial^2 u}{\partial x^2} + \frac{\partial^2 u}{\partial y^2} + \frac{\partial^2 u}{\partial z^2}\right] - \frac{1}{\rho}\left[\frac{\partial(\overline{u'u'})}{\partial x} + \frac{\partial(\overline{v'u'})}{\partial y} + \frac{\partial(\overline{w'u'})}{\partial z}\right] + g_x, \tag{21}$$

$$\vec{u}\cdot\vec{\nabla}(\hat{v}) = -\frac{1}{\rho}\frac{\partial p}{\partial y} + \nu\left[\frac{\partial^2 \hat{v}}{\partial x^2} + \frac{\partial^2 \hat{v}}{\partial y^2} + \frac{\partial^2 \hat{v}}{\partial z^2}\right] - \frac{1}{\rho}\left[\frac{\partial(\overline{u'v'})}{\partial x} + \frac{\partial(\overline{v'v'})}{\partial y} + \frac{\partial(\overline{w'v'})}{\partial z}\right] + g_y, \tag{22}$$

$$\vec{u}\cdot\vec{\nabla}(w) = -\frac{1}{\rho}\frac{\partial p}{\partial z} + \nu\left[\frac{\partial^2 w}{\partial x^2} + \frac{\partial^2 w}{\partial y^2} + \frac{\partial^2 w}{\partial z^2}\right] - \frac{1}{\rho}\left[\frac{\partial(\overline{u'w'})}{\partial x} + \frac{\partial(\overline{v'w'})}{\partial y} + \frac{\partial(\overline{w'w'})}{\partial z}\right] + g_z, \tag{23}$$

$$\frac{\partial\left(\rho\kappa u_i\right)}{\partial x_i} = \frac{\partial}{\partial x_j}\left[\left(\mu + \frac{\mu_t}{\sigma_\kappa}\right)\frac{\partial\kappa}{\partial x_j}\right] + G_k - \rho\varepsilon, \tag{24}$$

$$\frac{\partial\left(\rho\varepsilon u_i\right)}{\partial x_i} = \frac{\partial}{\partial x_j}\left[\left(\mu + \frac{\mu_t}{\sigma_\varepsilon}\right)\frac{\partial\varepsilon}{\partial x_j}\right] + C_{1\varepsilon}\frac{\varepsilon}{\kappa}(G_\kappa) - C_{2\varepsilon}\rho\frac{\varepsilon^2}{\kappa}, \tag{25}$$

where $\vec{u} = (u, \hat{v}, w)$. The MRF methodology calls for the splitting of the computational domain into two clearly distinctive regions on which the computations for the fluid flow will be performed. First, the RRF region, which is located in the inner part of the domain, consists of a cylinder-like surface directly attached to the impeller-shaft array (Figure 3.4). Apart from the splitting, another characteristic feature for this methodology, is that the reference frame is set to spin at the same angular velocity as the impeller. The second region, i.e., SRF, comprising the remainder of the computational domain, a laboratory (stationary) reference frame is used.

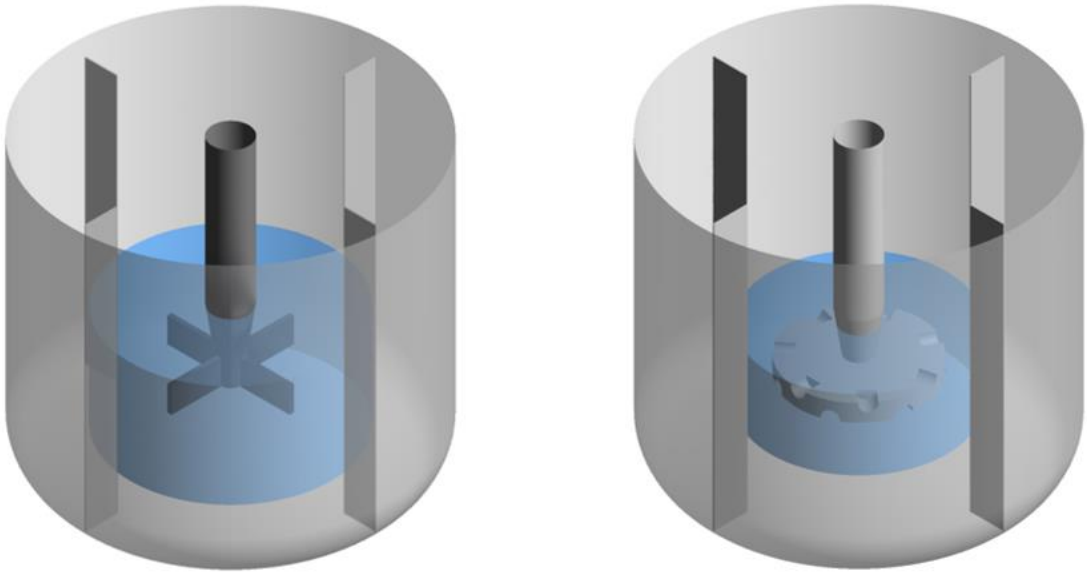

Figure 3.4 RRF region (blue) attached to each of the impellers employed in this research work: a) four flat-blade turbine, b) Norstone®

For the reference frame spinning within the RRF, this would yield a new form for the momentum (1)-(4) and equations (8)-(11) through the transformation:

$$\vec{u} = \vec{v} - \vec{\omega r}, \tag{26}$$

this way, the momentum equations will include two new additional terms, namely the centrifugal and Coriolis force (Glover et al., 2007):

$$F_{cor} = -2\rho\omega \times u, \tag{27}$$

$$F_{cent} = -\rho\omega \times (\omega \times r), \tag{28}$$

where ω is the angular velocity (constant) and $\vec{r}$ is the position vector. The information coming out of the computations within the RRF domain, then have to be forwarded to the SRF domain through boundary conditions at the interface for all flow properties, this requires an iterative process between both regions to achieve a converged solution (Sommerfeld et al., 2004), in addition to this, cell nodes that are common to both adjacent regions (RRF and SRF) will help to improve data transfer process, this by means of the construction of a conformal mesh.

3.2.6 The Finite Volume Method (FVM).

Computer simulations conducted in this research work are based on the employment of the finite volume method (FVM), which is a direct result of the divergence theorem (Protter et al., 1997; Spiegel, 1959; Spivak, 2018) (Appendix A). In order to illuminate the advantages of employing the results of this theorem in the realm of CFD, let us consider a bounded region in R^3 on which a mesh comprised by hexahedrons is embedded. Moreover, let us construct this mesh by performing a partition so fine that these hexahedrons are represented by cubes (see Figure 3.5), each of which is placed in such a manner that all its faces are in direct contact with other identical cubes.

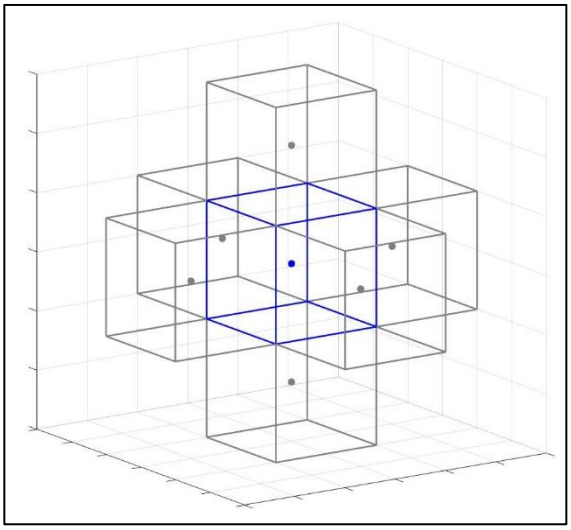

Figure 3.5 Cubes forming the partition in R^3 each of which represents the bounded region Ω.

In addition, let us assume that all these cubes have the same length (δ) and are represented by their centroid (filled ●) whose coordinates (x, y, z) are known. Furthermore, for instance, if the vector field $\vec{F}$ has the same direction as the velocity component u, then for the consecutive analysis (*the same analysis applies for the components v and w*) it can be considered exclusively the arrangement of cubes showed in Figure 3.6

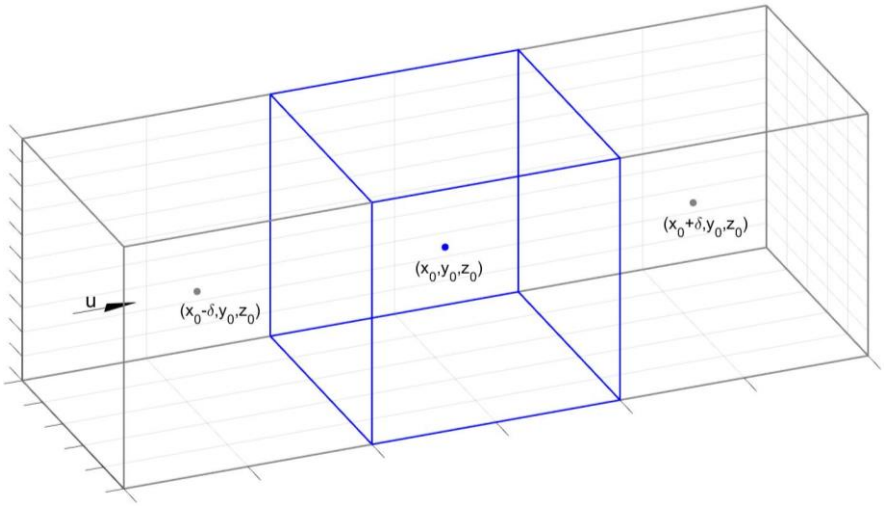

Figure 3.6 Arrangement of cubes aligned according to the direction of vector u

then, the vector field $\vec{F}$ in equations A2 and A3 can be replace by the velocity component u as follows:

$$\int_V \frac{d}{dx_i}\cdot(u)\,dV = \int_A \overrightarrow{n_{x_i}}\cdot(u)\,dA, \tag{29}$$

$$\int_V \frac{d^2}{dx_i^2}(u)dV = \int_A \overrightarrow{n_{x_i}}\cdot\left[\frac{d}{dx}(u)\right]dA, \tag{30}$$

noticing that both u and $\overrightarrow{n_{x_i}}$ are parallel, then on one hand we have:

$$\overrightarrow{n_{x_i}}\cdot(u) = \left\|\overrightarrow{n_{x_i}}\right\|\cdot\|u\|\cdot\cos(0^\circ),$$
$$\overrightarrow{n_{x_i}}\cdot(u) = (1)\cdot(u)\cdot(1),$$
$$\overrightarrow{n_{x_i}}\cdot(u) = u,$$

and on the other hand:

$$\overrightarrow{n_{x_i}}\cdot\left[\frac{d}{dx}(u)\right] = \left\|\overrightarrow{n_{x_i}}\right\|\cdot\left\|\frac{d}{dx}(u)\right\|\cdot\cos(0^\circ),$$
$$\overrightarrow{n_{x_i}}\cdot\left[\frac{d}{dx}(u)\right] = (1)\cdot\left(\frac{d}{dx}(u)\right)\cdot(1),$$
$$\overrightarrow{n_{x_i}}\cdot\left[\frac{d}{dx}(u)\right] = \frac{d}{dx}(u),$$

then, equations (29) and (30) can be simplified to:

$$\int_V \frac{d}{dx_i}\cdot(u)\,dV = \int_A u\,dA, \tag{31}$$

$$\int_V \frac{d^2}{dx_i^2}(u)dV = \int_A \frac{d}{dx}(u)dA. \tag{32}$$

From here, the surface integrals present in equations (31) and (32) can be approximated by means of the fundamental theorem of calculus (Apostol, 2007; Spivak, 1980). Noticing that

these integrals are going to be evaluated in the surfaces of the blue cube (see Figure 3.6) located at x_0-(δ/2) and x_0+(δ/2), respectively, then:

$$\int_A u dA = (uA)_{x_0+(\delta/2)} - (uA)_{x_0-(\delta/2)}, \tag{33}$$

$$\int_A \frac{du}{dx} dA = (A\frac{du}{dx})_{x_0+(\delta/2)} - (A\frac{du}{dx})_{x_0-(\delta/2)}, \tag{34}$$

considering that:

$$A_{x_0+(\delta/2)} = A_{x_0-(\delta/2)} = A,$$

then

$$\int_A u dA = A\left[u_{x_0+(\delta/2)} - u_{x_0-(\delta/2)}\right], \tag{35}$$

$$\int_A \frac{du}{dx} dA = A\left[\frac{du}{dx}_{x_0+(\delta/2)} - \frac{du}{dx}_{x_0-(\delta/2)}\right]. \tag{36}$$

3.2.7 Numerical estimators and accuracy.

The applicability of equations (35) and (36) is subjected to finding suitable expressions for the velocity component u and the derivative $\frac{du}{dx}$ at locations $x_0 \pm \delta/2$, where two lateral faces of the bounded cube showed in Figure 3.6 are located. By inspecting this same figure, a simple expression for u can be stablished by taking the average of the two neighboring values of u located at $x_0 \pm \delta$ as follows:

$$u_{x_0+\frac{\delta}{2}} = \frac{u_{x_0} + u_{x_0+\delta}}{2}, \tag{37}$$

$$u_{x_0-\frac{\delta}{2}} = \frac{u_{x_0} + u_{x_0-\delta}}{2}. \tag{38}$$

In the case of the derivatives $\frac{du}{dx}$ at locations $x_0 \pm \delta/2$ the procedure of finding approximations turns out to be a bit more elaborated. By considering a Taylor series expansion (Appendix B) of *u* in a neighborhood of x_0 (containing both $x_0+\delta$ and $x_0-\delta$) it can be shown that a good estimator for $\frac{du}{dx}$ is:

$$\frac{du(x_0 + \frac{\delta}{2})}{dx} \cong \frac{u(x_0 + \delta) - u(x_0)}{\delta}, \tag{39}$$

$$\frac{du(x_0 - \frac{\delta}{2})}{dx} \cong \frac{u(x_0) - u(x_0 - \delta)}{\delta}, \tag{40}$$

both expressions yield an error of order $O(\delta/2)^2$ for the derivative $\frac{du}{dx}$, while for the estimators represented by equations (37) and (38) the error has and order of $O(\delta^2)$ (Appendix C).

3.2.8 The quadratic interpolation for convective kinetics (QUICK) scheme.

It turns out that there exists a more accurate expression for the component *u* ($O(\delta^2) \rightarrow O(\delta^3)$) while retaining the same form and error order for its derivative $\frac{du}{dx}$. The quadratic upstream interpolation for convective kinetics (QUICK) (Appendix D) proposed by Leonard (1979), performs a second order polynomial fitting for any set of consecutive points ($x_{0-\delta}, x_0, x_{0+\delta}$) in order to compute *u* as follows:

$$u_{x_0+\frac{\delta}{2}} = -\frac{1}{8}u_{x_0-\delta} + \frac{6}{8}u_{x_0} + \frac{3}{8}u_{x_0+\delta}. \tag{41}$$

Although possessing a high order convergence of $O(\delta^3)$, this second order polynomial construction process is not the only fitting that can be imposed in a neighborhood of the intermediate point $x_0 + \frac{\delta}{2}$. Jing et al. (2006) proposed a third-degree polynomial fitting whose error order $O(\delta^4)$ surpasses that of QUICK. It makes perfect sense to believe that by constructing polynomials of higher order than those proposed by Leonard (1979) and Jing et al. (2006), better and more accurate expression for the component u can be obtained. This in principle is absolutely true, however, it should be noted that this construction process has a price in exchange for the high accuracy sought. As it is explained in Appendix D, the linear system of equations that needed to be solved in order to compute the coefficients $A, B, C,$ for the second order polynomial, takes into account finding the inverse of a square matrix which in turn according to the accuracy sought, will increase its size, thus demanding extra additional computing effort in order to find its inverse, up to the point where more robust algorithms (Bender et al., 2002; Macon et al., 1958; Spitzbart et al., 1957; Turner, 1966) might be employed. This deterrence to develop processes leading to polynomial fitting with accuracy greater than $O(\delta^3)$ or even $O(\delta^4)$, should be take it as an opportunity to consider the fact that by constructing finer partitions of the computational domain while maintaining (39), (40) and (41) as the estimators of $\frac{du}{dx}$ and u, affordable and reliable numerical approximations can be obtained for a stirred-tank system as it was reported previously by Deglon et al. (2006). For instance, let us consider two consecutive points x_0 and $x_{0+\delta}$ separated by a distance not bigger than δ, i.e.,

$$\left| x_0 - x_{0+\delta} \right| \leq \delta,$$

generating finer grids means that $\delta \to 0$ as a result of increasing the number of nodes embedded in the grid. A direct consequence is that from equations (39) and (40)

$$\frac{du(x_0+\frac{\delta}{2})}{dx}=\lim_{\delta\to 0}\frac{u(x_0+\delta)-u(x_0)}{\delta}, \tag{42}$$

$$\frac{du(x_0-\frac{\delta}{2})}{dx}=\lim_{\delta\to 0}\frac{u(x_0)-u(x_0-\delta)}{\delta}, \tag{43}$$

and on the other hand:

$$\lim_{\delta\to 0}\left|\left(-\frac{1}{8}u_{x_0-\delta}+\frac{6}{8}u_{x_0}+\frac{3}{8}u_{x_0+\delta}\right)-u_{x_0+\frac{\delta}{2}}\right|\le\lim_{\delta\to 0}\left\|\left[O(\delta^3)\right]\right\|=0, \tag{44}$$

meaning that the second order polynomial approximation $\left(-\frac{1}{8}u_{x_0-\delta}+\frac{6}{8}u_{x_0}+\frac{3}{8}u_{x_0+\delta}\right)$ approaches to $u_{x_0+\frac{\delta}{2}}$ at a rate much more faster than δ approaches to zero ($\delta\to 0$). The mathematical analysis presented here is conclusive, it demonstrates the fact that the estimators (41), (42) and (43) will have the ability to compute the exact values of all linear operators embedded in the set of second order partial differential equations (1)-(4) and (8)-(11), provided that the partition accounting for the digital replicas is so fine that an infinite number of points comprise it. However, the previous proposal has proved to be so far unfeasible. The only way to generate an infinite number of grid points will require a computer architecture that in one hand has no limits to memory storage and on the other hand that possess a great ability to process faster than ever imagined this large amount of data. Today, those systems still do not exist nor there is certainty that they will.

3.3 Mesh independence analysis

Since it is unpractical and computationally unfeasible constructing limitless finer partitions out of denser meshes (*more grid points*), then it seems reasonable to think that at least it can be assembled a mesh comprising a sufficient number of grid points capable to perform numerical iterations with sufficient accuracy by still procuring (42), (43) and (44) to hold true. The process by which it can be found this sufficient dense mesh is called mesh independence analysis, and calls for the construction of several meshes (*not too many*) with different number of nodal points and subject all of them to numerical iterations until convergence criteria is met. The results computed for each of these meshes are then thoroughly analyzed in order to obtain variations not greater than 5% between the numerical results yielded by two consecutive and further meshes. Once located the first mesh fulfilling this criterion, then this can be considered as the most recommended mesh containing a sufficient number of nodal points capable to procure (42), (43) and (44). To have a clearer picture of this process, let us consider the two impellers employed in this work (see Figure 3.1), to which their corresponding meshes were built as it is shown in Figure 3.7

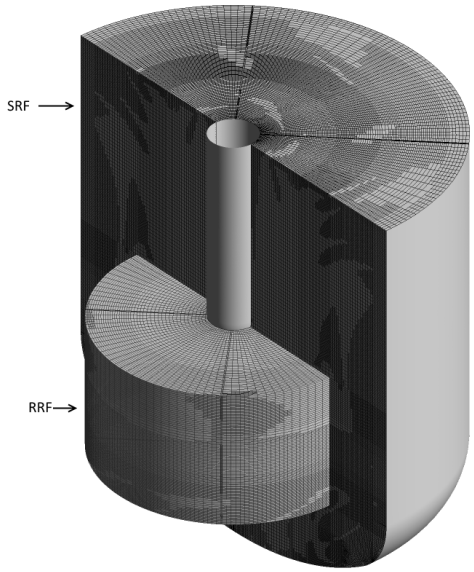

Figure 3.7 Schematic of a typical mesh employed in computer simulations for the two impellers.

From the previous figure, it can be seen that all meshes constructed were fragmented into two regions (SRF and RRF) as demanded by the MRF approach. The innermost region (RRF) was further subdivided into other seven different regions V1 up to V6 plus an extra one, this with the objective of varying the size of the RRF region in further computer simulations. In the case of the four flat-blade turbine, the extra seventh region was defined by the blades sweep volume (BSV) (Figure 3.8a), whereas in the case for the Norstone® impeller the extra seventh region was defined by the volume swept by the impeller grooves (VSG) (Figure 3.8b).

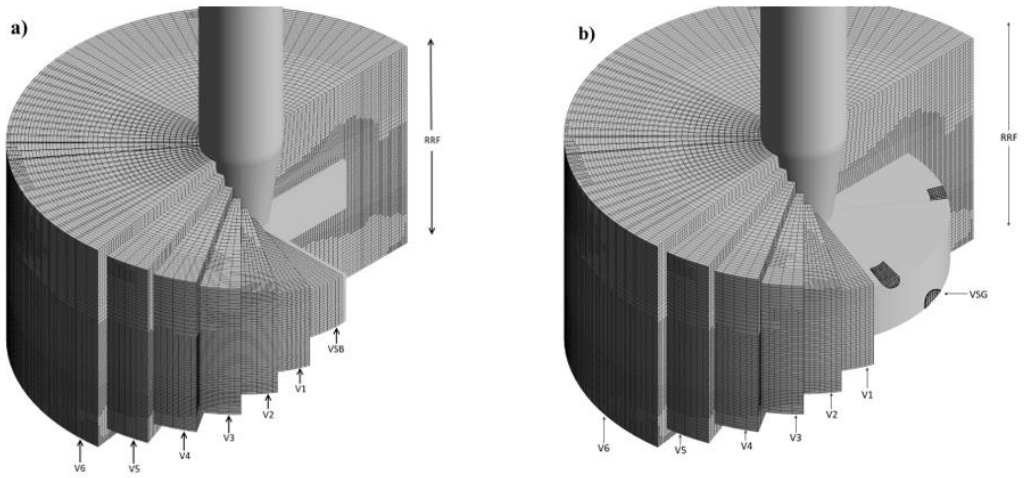

Figure 3.8 Splitting of the RRF region for the impellers: a) four flat-blade turbine, b) Norstone® impeller

The manner in which volumes V1 up to V6 were constructed was according to the following rule: volume V1 is the region immediately surrounding BSV in the case of the four flat-blade turbine and VSG in the case of the Norstone® impeller. Volumes placed away from V1, (i.e., from V2 up to V6) were successively deployed there to enclose the previous one. This lead to the construction of the different sizes for the RRF domain in both impellers as follows: RRF1=BSV+V1, RRF2=BSV+V1+V2, successively, up to RRF6=BSV+V1+V2+V3+V4+V5+V6 in the case for the four flat-blade turbine, and RRF1=VSG+V1, RRF2= VSG +V1+V2, successively, up to RRF6= VSG +V1+V2+V3+V4+V5+V6, in the case for the Norstone® impeller. It is worth to mention that V1 is different from the others in the sense that its surface is separated from BSV(VSG) surface at a distance corresponding to W/3 in all directions (where W, the impeller's width

is 10.2 mm for the four flat-blade turbine and 7 mm for the Norstone®). From V2 to V6 all their corresponding surfaces were located at a distance corresponding to W/4 from the previous one. With regards to the particular size of V1, this was chosen by trial and error to avoid the formation of non-hexahedral cells in this region. The boundary present between all adjacent regions, i.e., BSV(VSG), V1 to V6, and SRF, was conformal, meaning that all cell nodes comprising these boundaries were coincident between adjacent regions, requiring no additional interpolation between them, resulting in enhancing accuracy over the numerical simulations.

In order to properly select the recommended mesh for each of the two impellers, a pair of initial coarse meshes (representing each impeller) consisting exclusively of hexahedrons were built by using ANSYS© Meshing module. Owing to its radial periodicity, only one-fourth part of the stirred-tank system equipped with the four flat-blade turbine was built, thus enabling to computer savings up to 75%, whereas for the stirred-tank system equipped with the Norstone® impeller, no computer savings were obtained due to its lack of periodicity. From these basic meshes, further refinement was conducted using ANSYS© Fluent 17.1, obtaining four meshes with different skewness (see Table 2) and densities (see Table 3) for each impeller. The refinement criteria employed was based on the maximum velocity gradients obtained when simulations were conducted considering the highest peripheral velocity evaluated in this study (1000 RPM). The working fluid employed in these simulations was water (ρ=998.5 kg/m^3, μ= 0.001 Pa-s), thus leading to a Reynolds number of Re=42946.

Table 3.2 . Maximum skewness allowed for the two systems

	Impeller	
	four flat-blade turbine	Norstone®
Maximum skewness allowed	0.88	0.9

Table 3.3 Different meshes considered and their corresponding densities.

Mesh	***Impeller***	***RRF***							***SRF***	***whole domain***
		BSV VSG	***V1***	***V2***	***V3***	***V4***	***V5***	***V6***		
1	four flat-blade turbine	3960	3960	8200	9992	11784	13576	15368	172020	241308
	Norstone®	31088	282075	27991	13921	10474	17876	19924	647052	1050401
2	four flat-blade turbine	20760	32133	21276	20219	22004	23355	24881	239843	404471
	Norstone®	69847	1250250	36531	18814	22969	30420	33469	829829	2292129
3	four flat-blade turbine	31309	50515	54393	41443	29438	30019	39161	697370	973648
	Norstone®	70057	1502462	42509	19633	24698	32814	35884	1322419	3050476
4	four flat-blade turbine	119782	102336	65271	78998	91010	100460	111744	1306594	1976195
	Norstone®	70064	1968102	152708	81499	71318	110108	125645	4192552	6771996

An extra action was taken in all meshes so as not to build them with an excessive number of nodal points. This consisted in the employment of standard wall functions to account for the high velocity gradients present in the solid walls of the stirred-tank system. In all simulations the coupled algorithm was employed to approximate pressure gradients present in the governing equations. All simulations conducted in this stage considered the full extent of the RRF, i.e., RRF=RRF6. Figure 3.9 presents numerical approximations of torque values computed along the shaft in the stirred-tank system equipped with either of the two impellers.

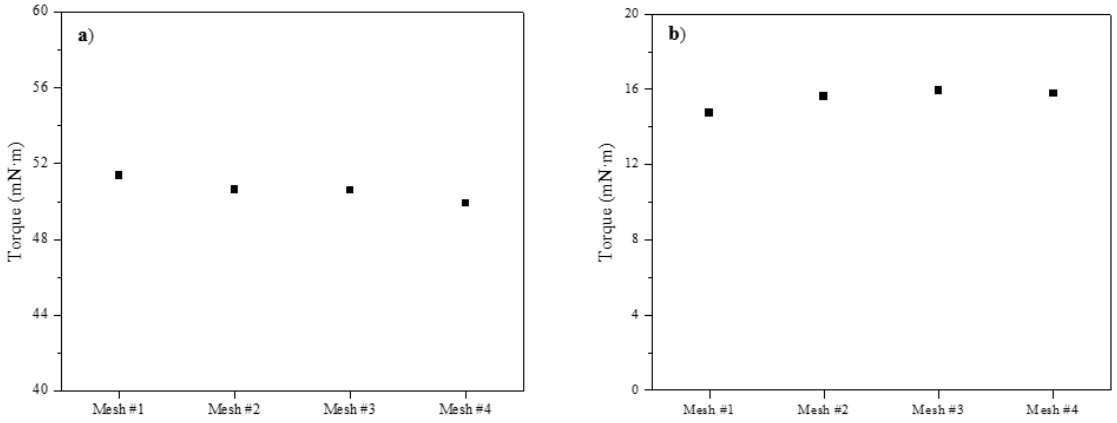

Figure 3.9 Numerical torque values computed for the two impellers as a function of mesh density: a) four flat-blade turbine, b) Norstone® impeller

If torque values were the only parameter to be judged in order to select the recommended mesh for each of the two impellers, then, in the case of the four flat-blade turbine, the Mesh #1 could have been considered the most recommended mesh, since its difference with respect to the densest mesh (Mesh #4) is less than 3%. In the case of the Norstone® impeller, the most recommended mesh would have been Mesh #2, since its difference with respect to the densest mesh (Mesh #4) is less than 2%. However, in order to verify their capability to predict with greater accuracy other hydrodynamical parameters such as the velocity magnitude ($\left\|\vec{u}\right\|_2 = \sqrt[2]{u^2+v^2+w^2}$), an extra analysis was conducted by studying the spatial distribution of this parameter over a straight line connecting directly the outer edge of each impeller to the inner surface of the baffle as is depicted in Figure 3.10. Measurements of the velocity magnitude were collected along these lines over 30 equally spaced points.

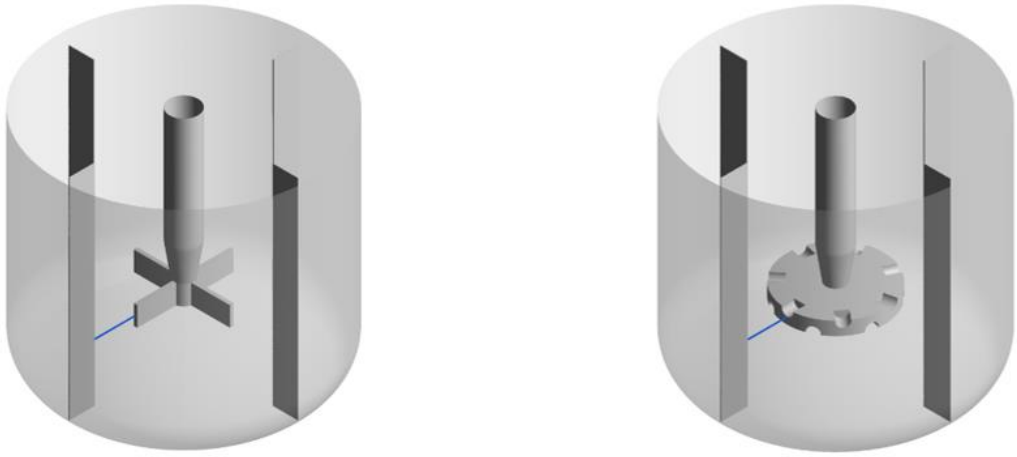

Figure 3.10 Straight radial lines depicted in blue for: a) four flat-blade turbine, b) Norstone® impeller

In the case of the stirred-tank equipped with the four flat-blade turbine, it can be verified based on Figure 3.11a, that the profile of the velocity magnitude computed when Mesh #1 (*previously selected*) is employed, presents a clear and visible difference with respect to the profile computed employing the densest Mesh #4, but moving forward to the point of considering the profile computed based on the Mesh #3, it can be seen that very good agreement is obtained. As a result, by declining Mesh #1 in favor of Mesh #3, more accurate predictions can be obtained for the stirred-tank system equipped with the Four flat pallet impeller.

In the case of the Norstone® impeller (Figure 3.11b), the panorama seems quite similar as the previous one. Comparing the velocity profiles between Mesh #2 (*previously selected*) and Mesh #4, it can be confirmed that a clear and visible difference is present between these, however, by declining Mesh #2 in favor of Mesh #3, it can be confirmed that there is very good agreement between this mesh and the densest one, this suggests that more accurate predictions can be obtained for the stirred-tank system equipped with the Norstone® impeller by selecting Mesh #3 as the representative for this stirred-tank system.

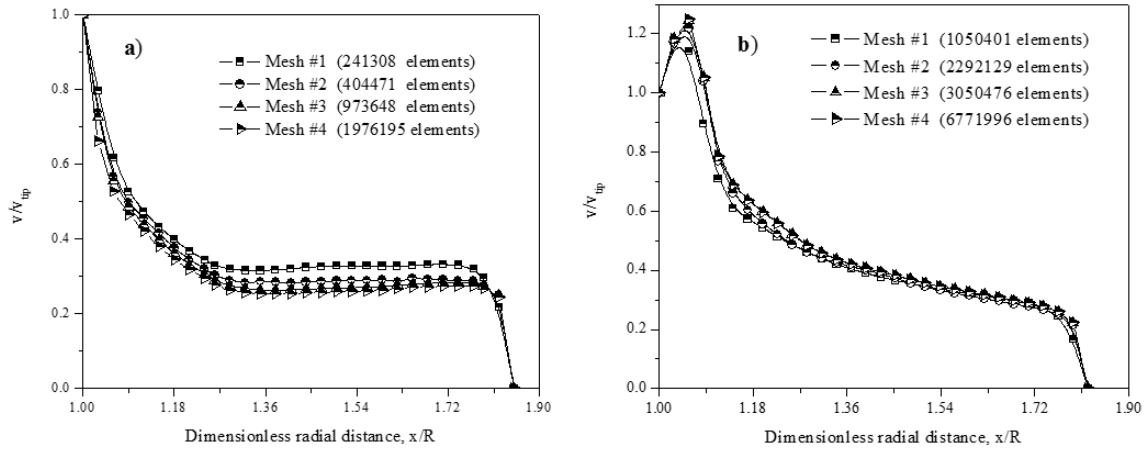

Figure 3.11 Dimensionless velocity magnitude values computed over the radial line for: a) four flat-blade turbine, b) Norstone® impeller.

From these results, the Meshes #3 were selected for both impellers as the most recommended meshes for further numerical simulations. Now the selected meshes have to be subjected to the final and by far the most important test in order to assess their capabilities to predict experimental measurements for real stirred-tank systems. To this end, numerical simulations were conducted considering Reynolds numbers in the intervals $1 \leq Re < 116$, and $21473 \geq Re \geq 42946$, corresponding to laminar flow and turbulent flow, respectively. Reynolds values corresponding to the interval $116 \leq Re < 21473$, represent the transitional flow regime. It should be noted that in this flow regime is not possible to employ a RANS-based turbulence model together with the MRF approach in order to correctly predict the non-stationary nature of the internal flow. The only option here is to conduct three-dimensional transient laminar simulations or DNS on extremely fine meshes (to fully capture the first appearances of eddies), in addition to the sliding-mesh method for modeling the impeller-baffle interaction

(J. Y. Murthy et al., 1994). Furthermore, these simulations must be conducted considering the entirety of the fluid domain. Executing DNS in the transitional flow regime for complex geometries such as stirred vessels can be translated into prolonged periods of time (*up to months*) to have the results ready, in addition to large storage requirements. For this reason, to report data in this flow regime is beyond the scope of this work.

From the simulations corresponding to the intervals $1 \leq Re < 116$ and $21473 \geq Re \geq 42946$, numerical torque values ($\Im$) were computed along the shaft for which either case the impeller was mounted on its end. These torque values were then converted to power number values according to the expression (Martínez-de Jesús et al., 2017):

$$N_P = \frac{2\pi\Im}{\rho N^2 D^5}. \tag{45}$$

Owing to the radial periodicity exhibited by the stirred-tank system equipped with the four flat pallet impeller, N_P numerical values were multiplied by a factor of 4. In order to verify the validity of the numerical results obtained through equation (45) for the two computer models, these were compared with those obtained from the lab-scale experiments explained in section 3.1.

4 RESULTS

4.1 CFD Model Validation

This chapter begins with a criticism on how well the digital replicas of the systems employed (figures 3.4 and 3.7) yield numerical results that accurately represent power number values obtained in the laboratory. To this end, the numerical simulations were conducted employing in both cases the selected Mesh #3, embedded with 973648 and 3050476 cells for the four flat-blade turbine and the Norstone® impeller, respectively. Figure 4.1 shows the results of comparing numerical values extracted from CFD simulations and those gathered from the laboratory-scale experiments (section 3.1). In general, it can be seen that there is very good agreement between both results, i.e., experimental and numerical power number values. From Figure 4.1a, it can be observed that a maximum error of 13.2% was obtained at Re=4.9 when the stirred-tank system equipped with the four flat-blade turbine is working in the laminar regime. The value for this particular error value might be attributed to the proximity of the torque readings to the resolution of the Futek® instrument at this particular Re number, for this reason, experimental Reynolds numbers below 4.9 were not consider in this study. In the case of the stirred-tank system equipped with the Norstone® impeller (Figure 4.1b) operating in the same regime, the largest error noticed was 10.7%. The standard deviation over 1500 experimental torque readings (see section 3.1) at each Re value is indicated as error bars in Fig. 4.1. It should be noted that a break in Re between 120 and 20000 was included.

Moving forward to Reynolds numbers covering the turbulent regime, it can be confirmed that there is very good agreement between numerical and experimental results for both systems. This high accuracy in the numerical predictions of N_P, yielded errors not bigger than 4.0% and 5.3% for the system equipped with the four flat-blade turbine and with Norstone® impeller, respectively.

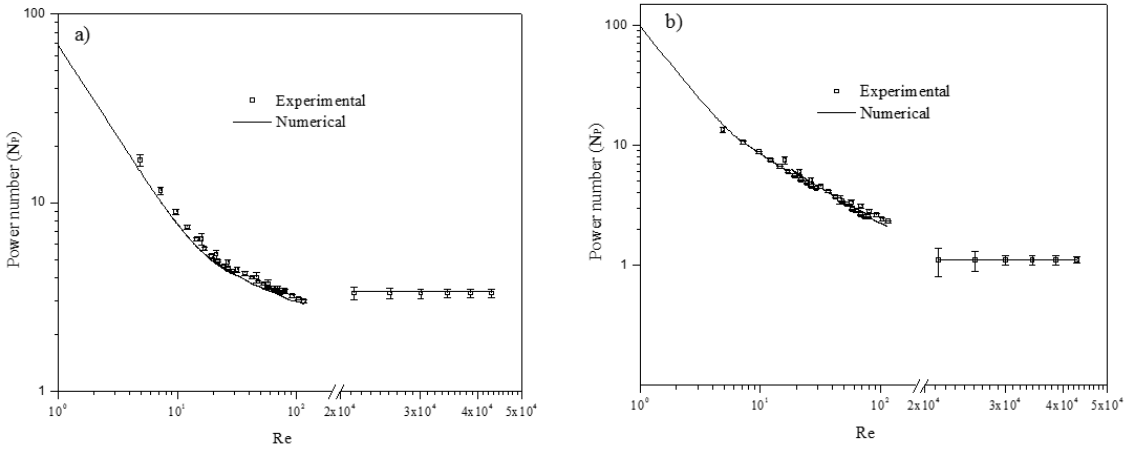

Figure 4.1 Comparison between experimental and power number values for: a) four flat-blade turbine, b) Norstone® impeller.

Overall, it can be concluded that there exists good agreement between power number values computed based on the digital replicas embedded with their corresponding number of cells, and those values gathered in the laboratory, thus validating the reliability and accuracy-procurement of the meshes employed.

4.2 RRF extensions considered

From this point, numerical simulations were conducted considering exclusively five Reynolds numbers representing laminar and turbulent flow. Those Re numbers can be consulted in table 4.1.

Table 4.1 Reynolds numbers evaluated representing different flow regimes.

Regime	Re considered
Laminar	4.9, 29.4, 115.9
Turbulent	21473, 42946

With regards to the size of the RRF region, six cases of study were considered each one representing a different extension for the RRF region surrounding the impeller. Table 4.2 presents the dimensionless extensions of the six regions employed in the CFD simulations, i.e., the radius and the height of the cylinder enclosing the impeller, normalized by the impeller radius.

Table 4.2 Dimensionless RRF extents simulated in this study

	RRF radius		RRF height	
Study case	four flat-blade turbine	Norstone® impeller	four flat-blade turbine	Norstone® impeller
RRF1	1.133	1.092	0.669	0.230
RRF2	1.234	1.161	0.870	0.299
RRF3	1.334	1.230	1.070	0.367
RRF4	1.435	1.299	1.270	0.436
RRF5	1.535	1.367	1.472	0.505
RRF6	1.635	1.436	1.673	0.574

Figure 4.2 shows a series of images exemplifying all study cases simulated considering the dimensionless RRF extents showed in Table 4.2. For simplicity it was decided to show them based on the stirred-tank system equipped with the four flat-blade turbine.

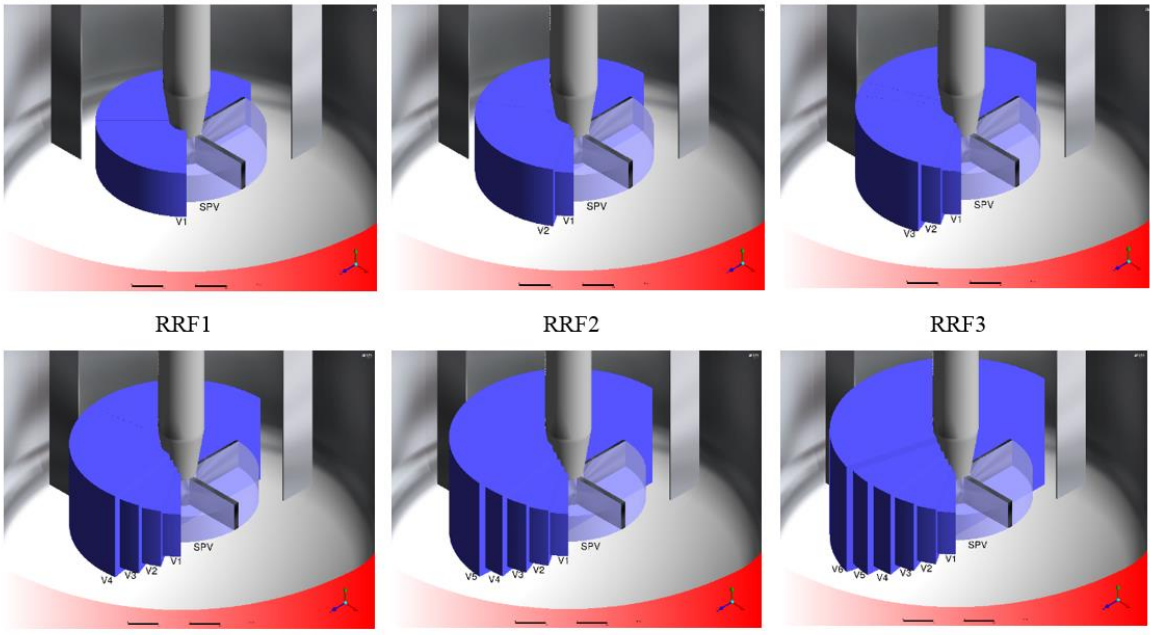

Figure 4.2 Dimensionless extensions for the RRF domain.

4.3 Hydrodynamical parameters

The results retrieved from numerical simulations, were examined in detail to quantify possible variations in the numerical approximations on power number and velocity magnitude profiles by imposing modifications on the dimension of the RRF region.

4.3.1 Power number (N_P)

The first approach of the examination process consisted in analyzing numerical approximations of the N_P for both impellers. Figure 4.3a shows the results for the stirred-tank system equipped with the four flat-blade turbine. Initially, it can be seen that for the lowest Re of 4.9 no appreciable differences exist in the N_P values as the size of the RRF increases, this particular result suggests that for Re numbers located in the creepy flow regime, an extension of the RRF equal to that of RRF1 will suffice. Moving forward to bigger Re numbers, for instance, at Re=29.4 an initial difference of 13% for computed N_P values existing between RRF1 and RRF6 can be reduced to less than 4% by declining RRF1 in favor of RRF3. In the case of Re=115.9, differences less than 4% between computed for N_P values arise when selecting RRF3 as the minimum size for the RRF. Moving beyond laminar flow conditions up to fully turbulent flow (i.e., Re of 31473 and 42946), a rather larger size than RRF3 needs to be considered in order to yield accurate representations for the N_P, in this case an extension equal to RRF5 will suffice. In light of this last particular result, it is worth to mention that by considering an extent for the RRF equal to RRF5 for all numerical simulations covering both flow regimes, the result will be accurate representations of N_P whatever the Re number under consideration.

On the other hand, the scenario is completely different for the stirred-tank system equipped with the Norstone® impeller. Considering the results showed in Figure 4.3b, it can be seen that regardless of the flow regime, no clear and visible differences exist in the computed N_P values as the extension for the RRF region increases from RFF1 up to RRF6, suggesting that for this impeller in particular, a RRF region matching the size of RRF1 will suffice for accurate and reliable numerical approximations.

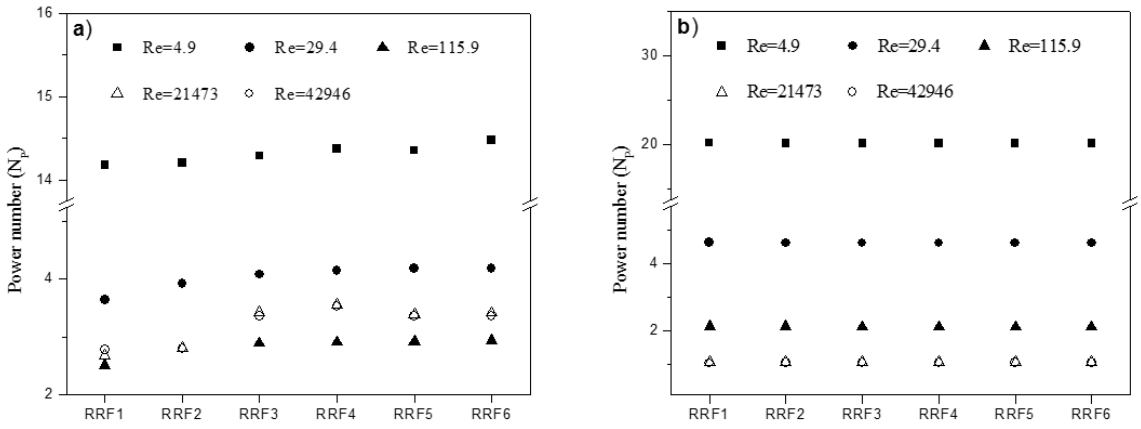

Figure 4.3 Numerical N_P values as a function of the RRF size for: a) four flat-blade turbine, b) Norstone®

Judging exclusively based on the results previously presented, then it would have been concluded that extensions RRF5 and RRF1 for the four flat-blade turbine and the Norstone® impeller, respectively, are the most recommended extension.

4.3.2 Velocity magnitude

In order to support or to discourage the validity of the previous selections, it was decided to conduct a rather more thorough analysis, this time by considering the hydrodynamical parameter velocity magnitude. As depicted in Figure 3.10, over the same radial line connecting each impeller outer edge with the baffle inner face, numerical velocity magnitude values were computed along the 30 points. As a result of the six cases of study considered, an equal number of profiles were obtained and then analyzed in order to detect discrepancies between them. Considering the profiles computed for the laminar flow regime represented by Figure 4.4, at first it can be seen that for the lowest Re number considered (Figure 4.4a) there is good agreement between all profiles computed, however by inspecting the cases corresponding to Re=29.4 (Figure 4.4b) and Re=115.9 (Figure 4.4c), respectively, it can be noticed that there exist significative differences between the profile representing RRF6 and those computed for RRF1, RRF2 and even for RRF3, but in the case of considering at least the profile corresponding to RRF4, then good resemblance exist between this particular profile and that corresponding to RRF6. This particular result suggests that for the laminar regime, an extension for the RRF equal to that of RRF4 will suffice.

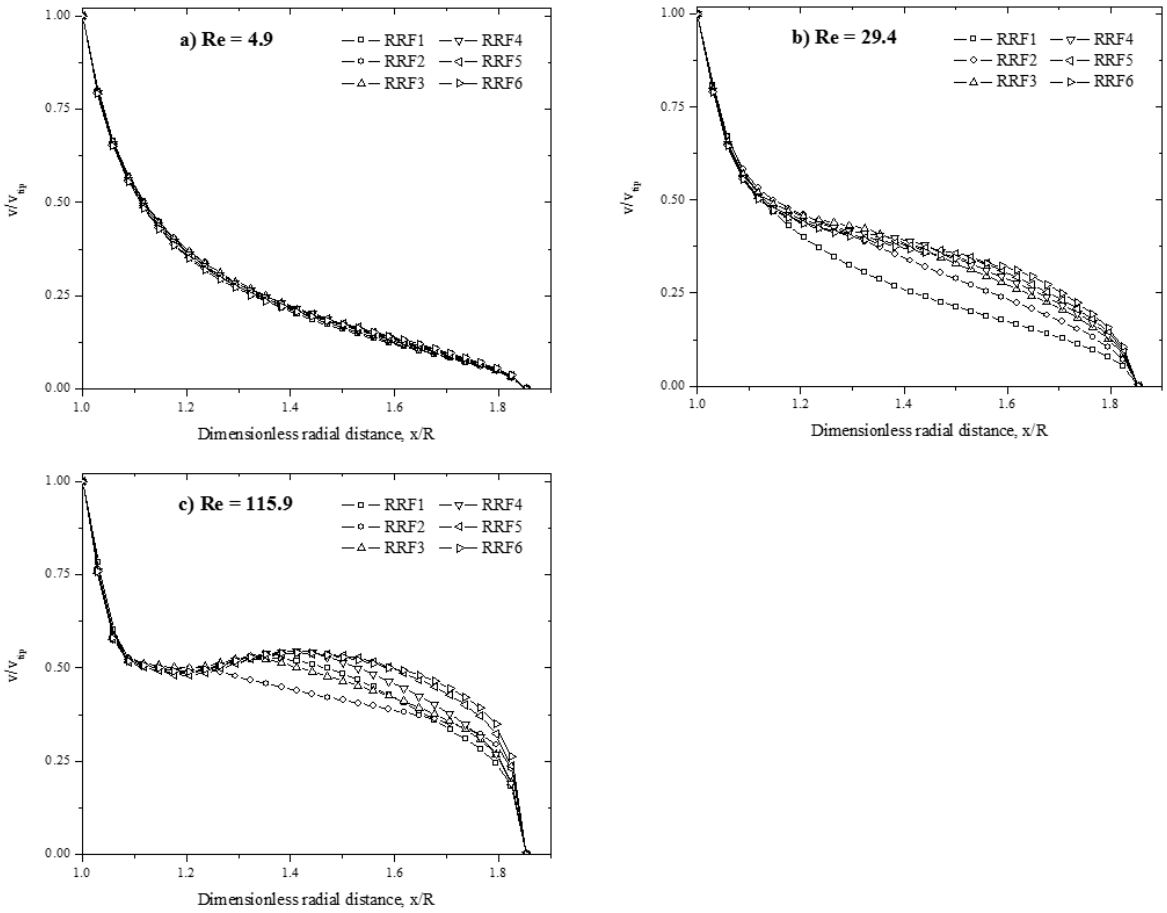

Figure 4.4 Dimensionless velocity magnitude along a radial line for the four flat-blade turbine operating in the laminar regime.

Shifting towards fully turbulent conditions, in Figure 4.5 can be consulted the results for the velocity magnitude profiles for Re=21473 and Re=42946. In both cases it can be noticed that for extensions corresponding to RRF1, RRF2, RRF3 and even for RRF4, significative differences can be found between their corresponding profiles and that computed for RRF6, however if selecting RRF5 as the recommended extension for RRF, a nearly perfect match will exist between both profiles (i.e., RRF5 and RRF6).

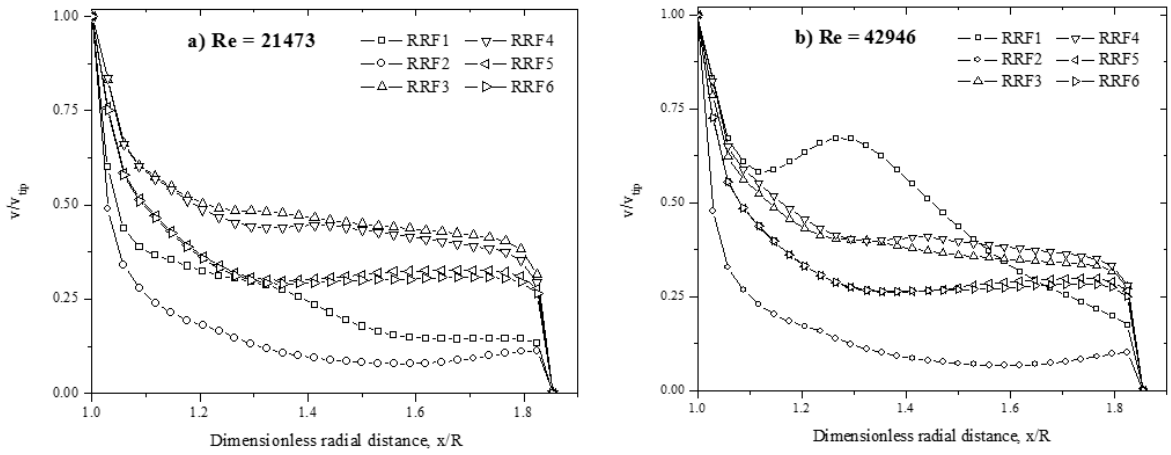

Figure 4.5 Dimensionless velocity magnitude along a radial line for the four flat-blade turbine operating in the turbulent regime.

It turns out that by maintaining this selection (i.e., RRF=RRF5), not only in the turbulent regime but in the laminar regime as well can be obtained accurate and reliable numerical approximations of this hydrodynamical parameter analyzed.

Shifting to the case of the stirred-tank equipped with the Norstone® impeller, a similar procedure can be developed and applied. Figure 4.6 shows the profiles computed exclusively for the laminar flow regime. Overall, it can be seen that there exists very good agreement between all curves, being the case represented by Figure 4.6a as the case on which there exist a nearly perfect match between all profiles. Apart from this particular case, the remaining two (i.e., Figure 4.6b and 4.6c) present slight deviations in the profiles computed. It is interesting to note that those deviations have clear zones on which they appear. In the case of Re=29.4 (Figure 4.6b), these deviations appear a little bit before the radial distance 1.3 and have a tendency to remain present before reaching the end of the radial line. In the case of Re=115.9 (Figure 4.6c), deviations appear right after the radial distance 1.0 and remain present somewhere in between distances 1.4 and 1.6.

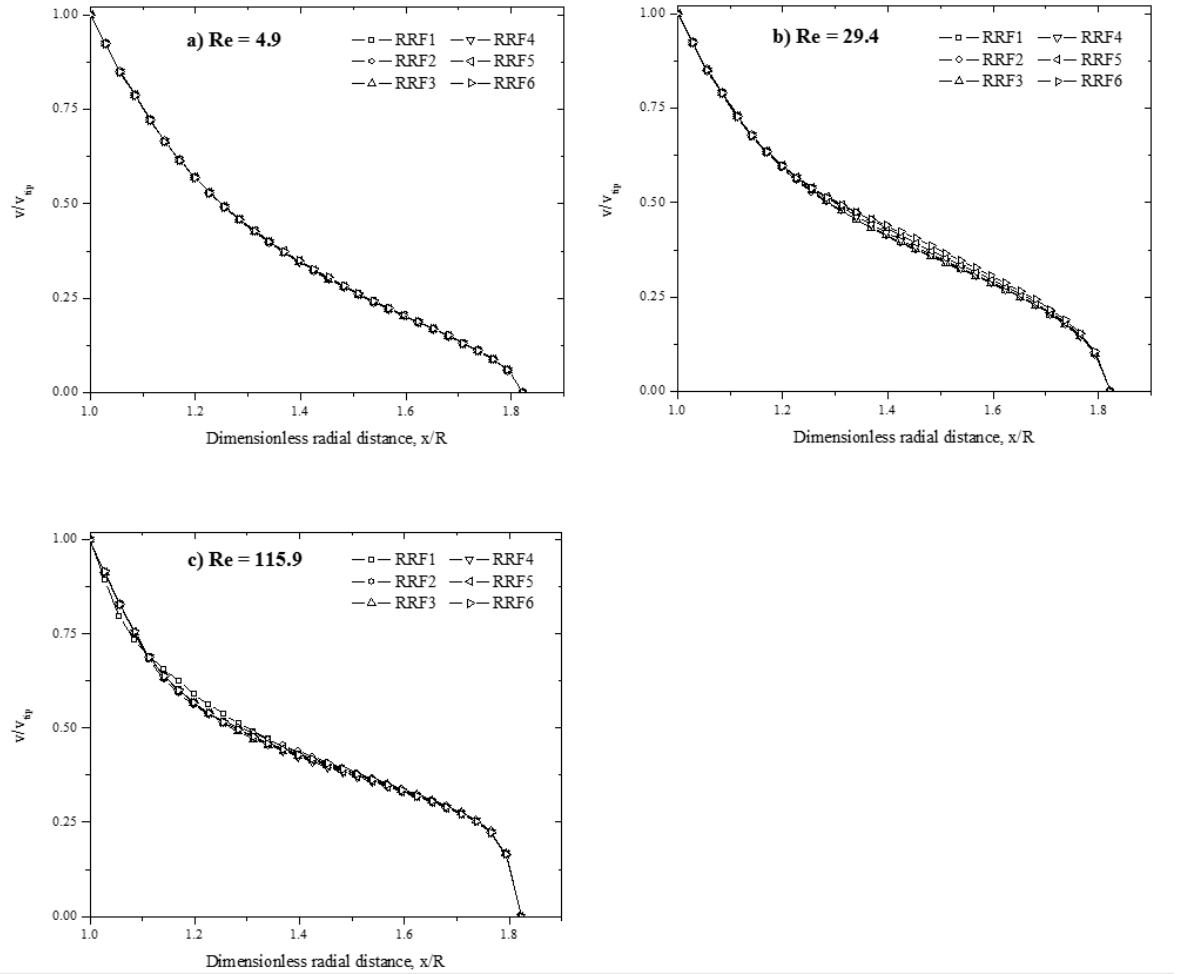

Figure 4.6 Dimensionless velocity magnitude along a radial line at y=0 (impeller midplane) for the Norstone® impeller operating in the laminar regime.

Moving forward to Re numbers representing turbulent flow conditions, a similar conclusion can be drawn as it was for the previous impeller. Based on the velocity magnitude profiles for Re=21473 (Figure 4.7a) and Re=42946 (Figure 4.7b), it can be demonstrated that for extensions corresponding to RRF1 up to RRF4, significative differences can be found between their corresponding profiles and that computed for RRF6, however by declining all the previous in favor of RRF5 as the recommended extension for RRF, good agreement between both profiles can be obtained (i.e., RRF5 and RRF6).

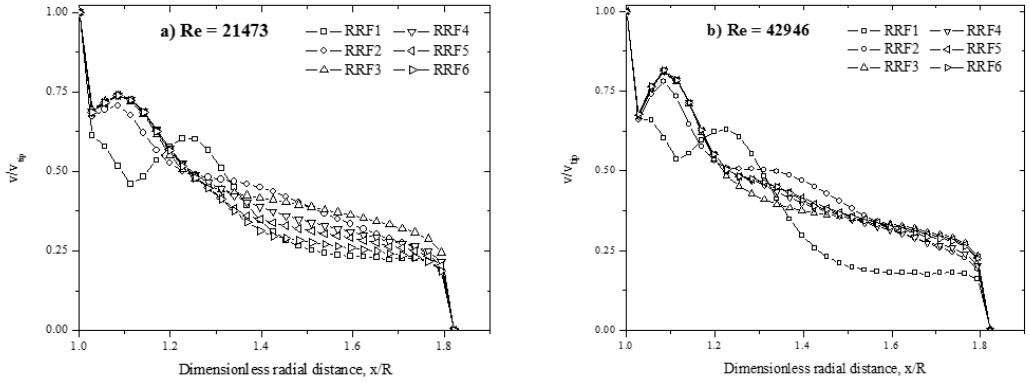

Figure 4.7 Dimensionless velocity magnitude along a radial line for the Norstone® impeller operating in the turbulent regime.

Up to this point in the current analysis, a partial conclusion can be stablished; this points to selecting in both cases (i.e., for both impellers) extensions for the RRF equal to RRF5 as the most recommended extension in order to obtain accurate and reliable numerical approximations, however, not only in this direction (i.e., radial) can the velocity magnitude profiles be analyzed. In order to investigate the behavior of the same profiles on a larger distance, an axial line evenly divided in 50 spaces connecting the free surface of the liquid to the bottom edge of the tank and passing through the impeller edge was drawn (see Figure 4.8).

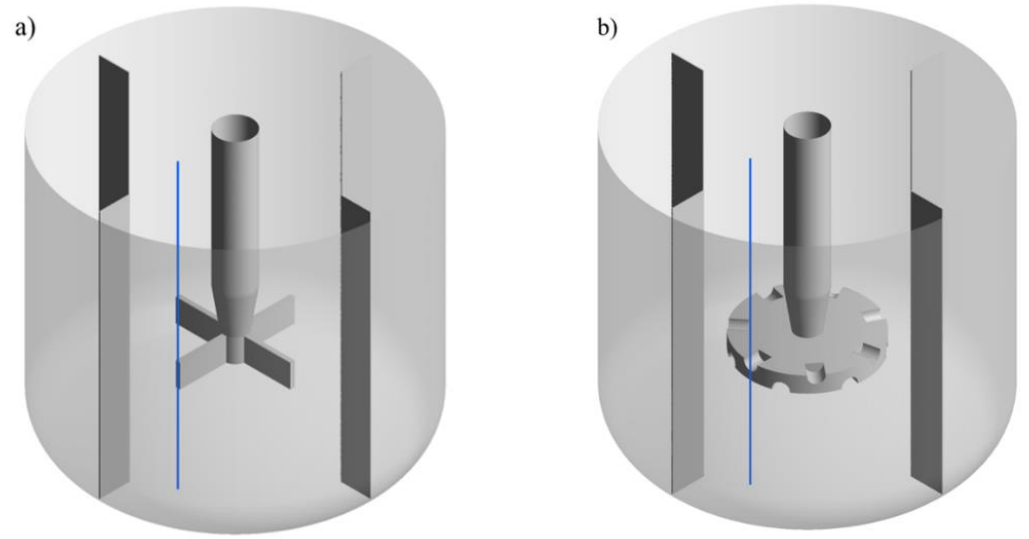

Figure 4.8 Straight axial lines depicted in blue for: a) four flat-blade turbine, b) Norstone® impeller

Similar to the case of radial lines, over these axial lines the profiles were computed and scrutinized in order to detect discrepancies between these.

In Figure 4.9 can be seen the results corresponding to the profiles computed for the stirred-tank system equipped with the four flat-blade turbine operating in the laminar regime. In general, it can be noticed that no clear and significant discrepancies can be detected on these approximations extracted along the vertical line as a result of conducting modifications on the size of the RRF region. Only slight disturbances located near the edges of the impeller blade ($y/R \approx \pm 0.3$) are present for these computed values at Re=29.4 (Figure 4.9b) and Re=115.9 (Figure 4.9c) for the cases when the RRF region is smaller than RRF3.

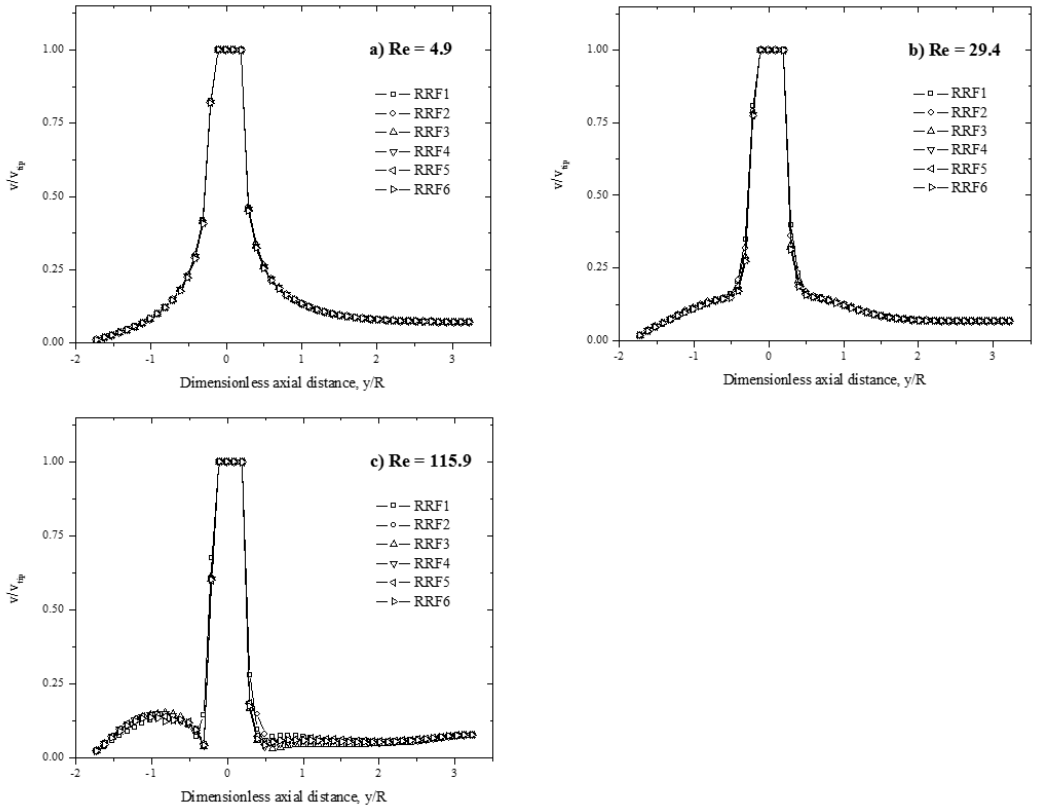

Figure 4.9 Dimensionless velocity magnitude along an axial line for the four flat-blade turbine operating in the laminar regime.

Figs. 4.10a and 4.10b depicted the results for Re=21473 and Re=42946, respectively. Based on these, it can be seen that there is a clear effect over the profiles when the size of the RRF region varies between RRF1 and RRF4. However, if the extension of the RRF region is enlarged to equal that of RRF5, as a result, there will be good agreement between this particular profile and that corresponding to RRF6.

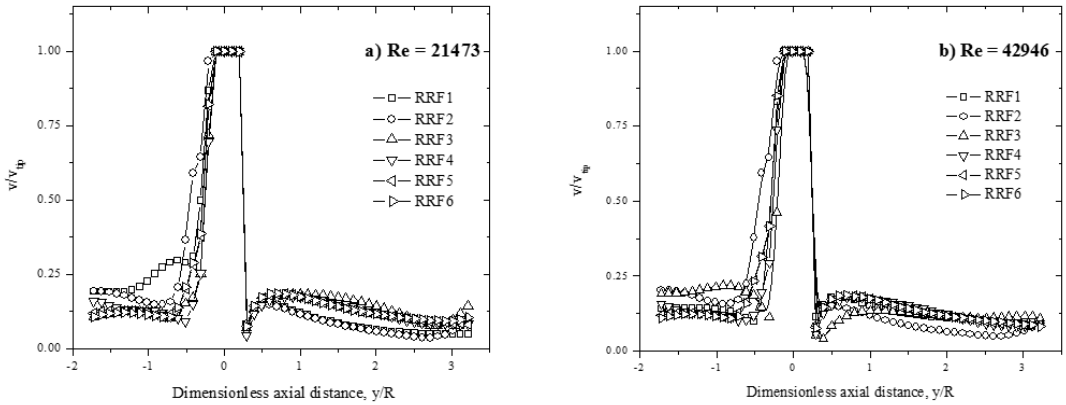

Figure 4.10 Dimensionless velocity magnitude along an axial line for the four flat-blade turbine operating in the laminar regime.

Turning our attention to the Norstone® impeller, the data representing velocity magnitude profiles measured over the axial line can be seen in Figure 4.11 and 4.12. In the case of laminar flow regime (Figure 4.11), in all of the Reynolds numbers depicted (Re=4.9, Re=29.4 and Re=115.9) it can be seen that there is very good agreement between all profiles showed, suggesting in particular that at this flow regime an increased in the extension of the RRF region will have a limited impact over the accuracy of the numerical approximations, thus ruling out the necessity for such enlargement.

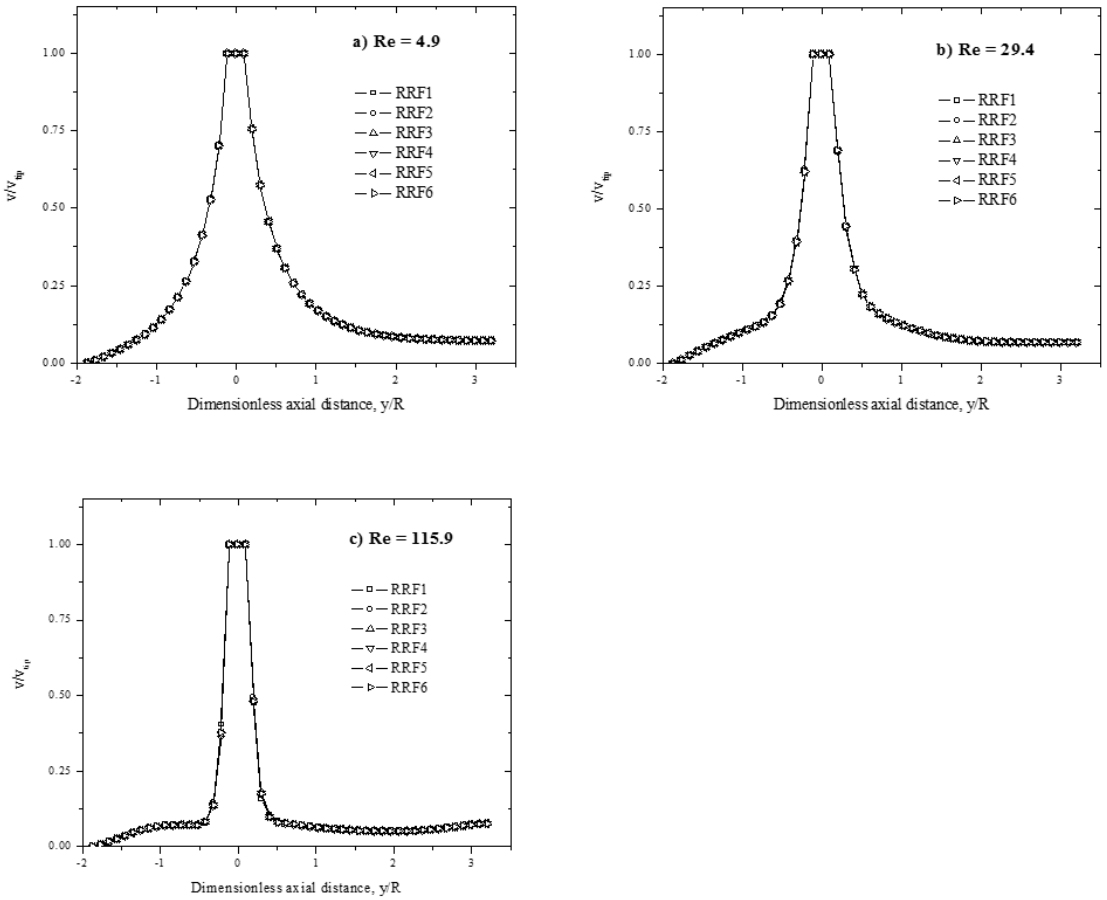

Figure 4.11 Dimensionless velocity magnitude along an axial line for the Norstone® impeller operating in the laminar regime.

Moving forward to Reynolds numbers representing turbulent flow conditions (Figure 4.12), similarly to the previous case presented, at first it would have appeared that an increase in the extension of the RRF domain would have represented a limited impact in the accuracy of the numerical approximation of the velocity magnitude profiles presented in figures 4.12a and 4.12b, thus ruling out the necessity for such enlargement. However, by inspecting thoroughly both pictures, it can be seen that significant discrepancies exist in the upper (4.12a) and lower tail (4.12b) of the profiles. It turns out that these discrepancies can be reduced drastically to the point on which they become undistinguishable by forcing the RRF region to increase its size to match that of the RRF5.

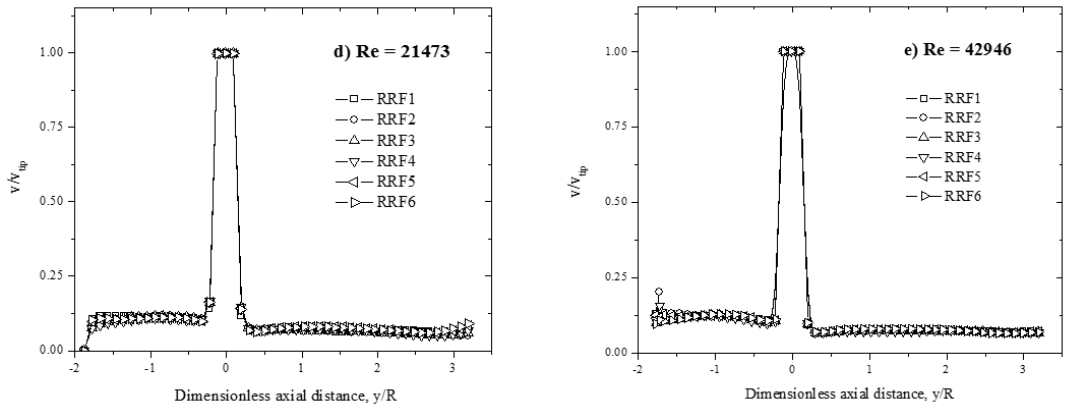

Figure 4.12 Dimensionless velocity magnitude along an axial line for the Norstone® impeller operating in the turbulent regime.

Up to this point in the current analysis, a partial conclusion can be stablished, this points to selecting in both cases (i.e., for both impellers) extensions for the RRF equal to RRF5 as the most recommended extension in order to obtain accurate and reliable numerical approximations. However, to assess the validity of the previous selection for the RRF region, a last step can be performed in order to be conclusive.

4.3.3 Shear rate

In Fig. 4.13 are showed average numerical values of shear rate computed in regions near the impeller (BSV and from V1 to V4, see Figure 3.8) for the stirred-tank system equipped with the four flat-blade turbine operating in the laminar regime. These values were computed as a function of the RRF-region size for the selected Re numbers: Re=4.9 (Fig. 4.13a), Re=29.4 (Fig. 4.13b) and Re=115.9 (Fig. 4.13c). It can be seen that for this flow regime, maximum shear rate values are located near the impeller, i.e., in BSV and V1. However, at the lowest Re number evaluated (Re=4.9), its maximum value is located in V1, whilst at Re=29.4 and Re=115.9, maximum values of shear rate induced by the impeller are located in the blades swept volume (BSV).

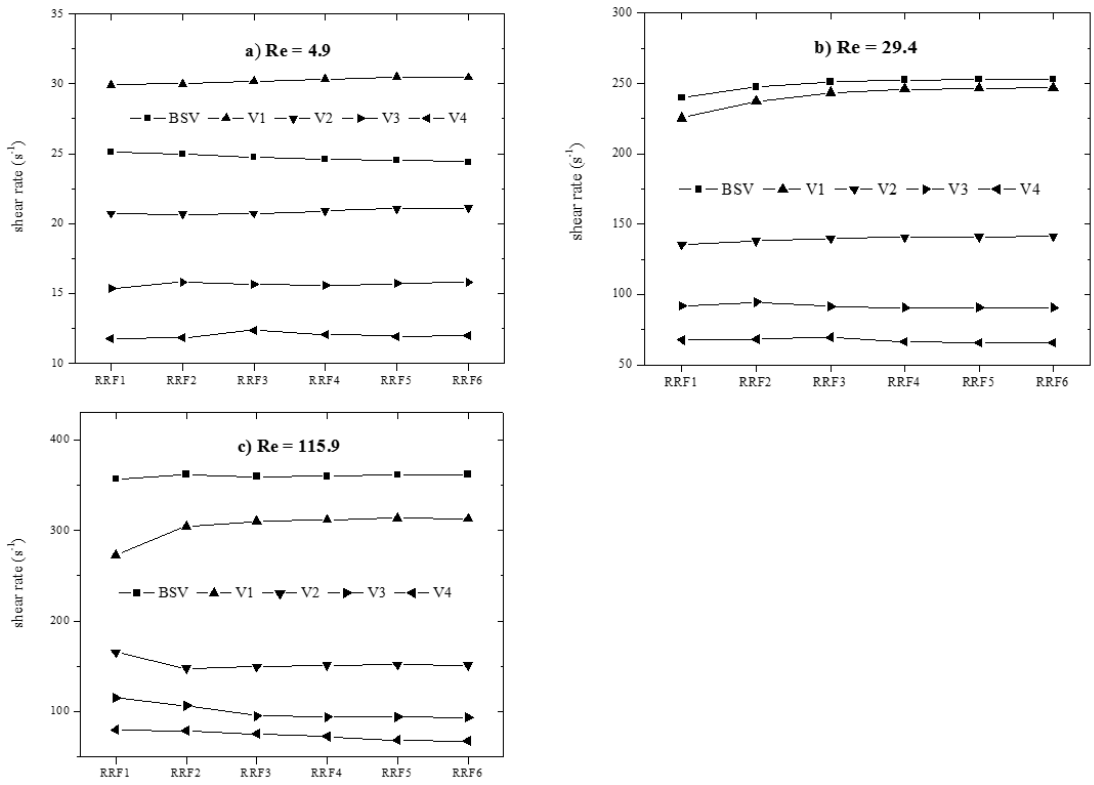

Figure 4.13 Average shear rate values in volumes near the impeller for the stirred-tank system equipped with the four flat-blade turbine operating in the laminar regime.

Moving forward to Reynolds numbers covering the turbulent regime, Figure 4.14 shows shear rate numerical values computed in the same regions. In resemblance to the laminar flow regime, here it can be seen that the highest shear rate values are located near the impeller, i.e., in BSV and V1, maintaining maximum values located in V1 region for both Reynolds numbers simulated in this flow regime: Re=21473 (Fig. 4.14a), Re=42946 (Fig. 4.14b). It is worth to mention that the similitude in the average shear rate values induced by the four flat-blade turbine operating at Re of 115.9 and 42946, comes from the fact that for both Reynolds number the same impeller speed (1000 rpm) was used (see Table 3.1).

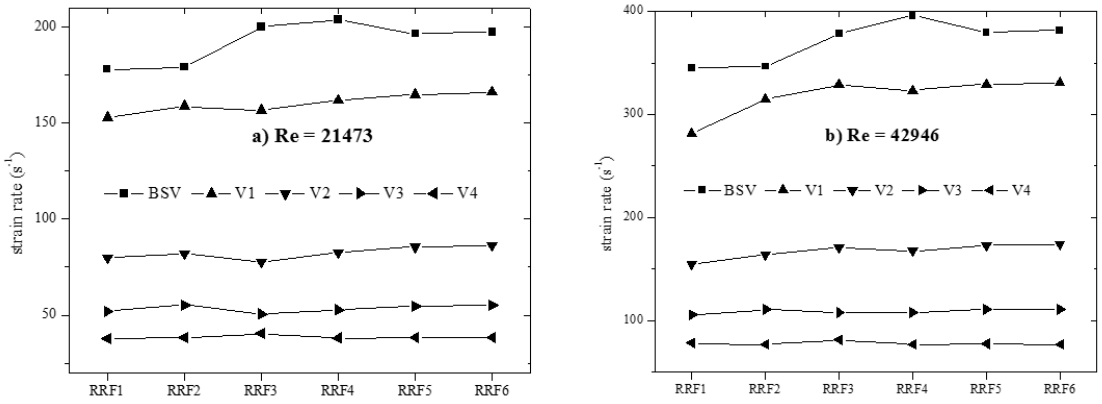

Figure 4.14 Average shear rate values in volumes near the impeller for the stirred-tank system equipped with four flat-blade turbine operating in the turbulent regime.

With regards to the effect of the size of the RRF region, based on both figures (Figure 4.13 and 4.14) it can be proposed that the minimum recommended extension for the RRF can be RRF5. With this selection, numerical values of shear rate will be accurate and well represented in the laminar and turbulent flow regimes.

Considering now the stirred-tank system equipped with the Norstone® impeller conducting mixing operations in the laminar flow regime, on figure 4.15 are showed average numerical values of shear rate. For this impeller, the VSG region (see Figure 3.8b) comprised the upper grooves and lower grooves regions. Similarly, these values were computed as a function of the RRF-region size for the selected Re numbers: Re=4.9 (Fig. 4.15a), Re=29.4 (Fig. 4.15b) and Re=115.9 (Fig. 4.15c).

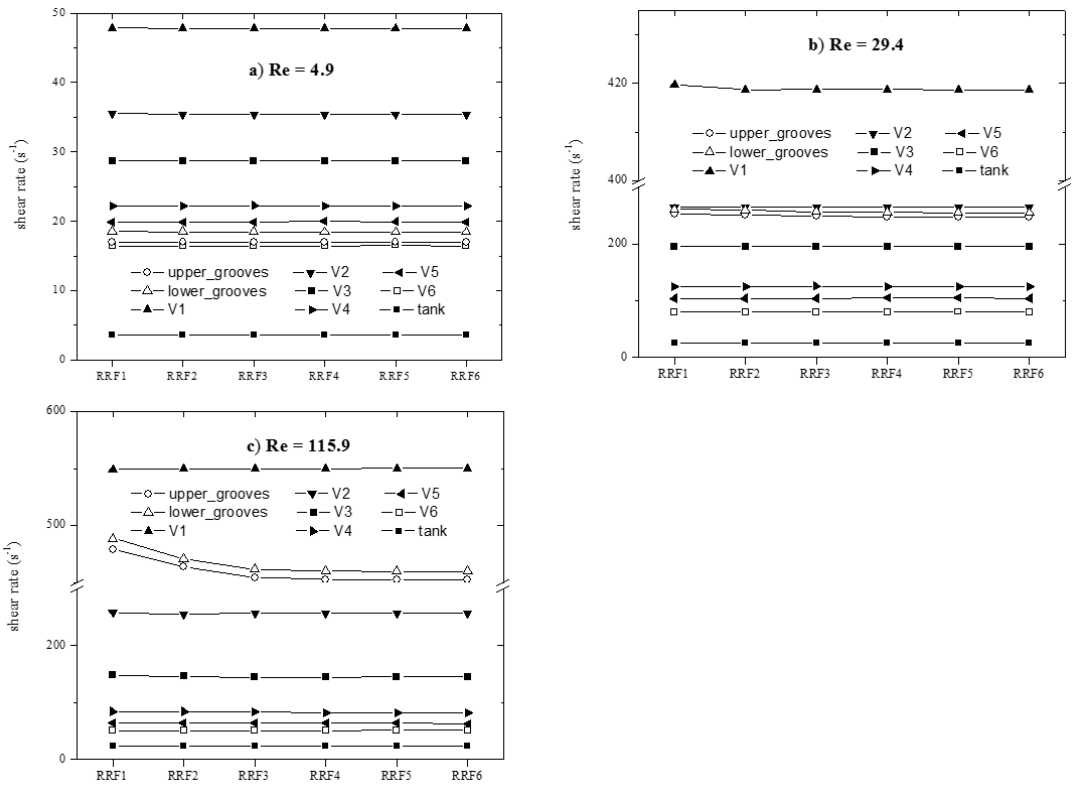

Figure 4.15 Average shear rate values in volumes near the impeller for the stirred-tank system equipped with the Norstone® impeller operating in the laminar regime.

For this flow regime, it can be noticed that the maximum values for the shear rate are located in V1. By inspecting the cases represented in figures 4.15a and 4.15b, it can be noticed that no significant differences are present in the computed values of shear rate, thus ruling out the necessity for an enlargement in the extension for the RRF region. Moving forward to the case represented in figure 4.15c, the scenario is different, it can be noticed that there exist significative variations for the parameter considered when the extension of the RRF region coincides with that of RRF1 or RRF2, however if RRF is extended at least as far as RRF3, accurate approximations will be obtained regardless of the volume considered within the stirred-tank system. Now considering Reynolds numbers covering the turbulent regime, Figure 4.16 shows computed shear rate numerical values. Contrary to the laminar flow regime, here it can be seen that the highest shear rate values are located in the upper grooves and lower grooves regions for both Reynolds numbers simulated in this flow regime: Re=21473 (Fig. 4.16a), Re=42946 (Fig. 4.16b).

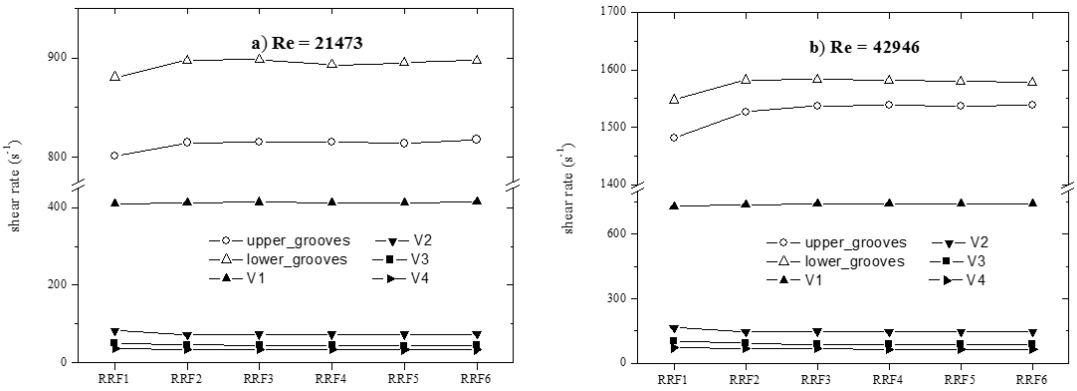

Figure 4.16 Average shear rate values in volumes near the impeller for the stirred-tank system equipped with the Norstone® impeller operating in the turbulent regime.

With regards to the effect of the size of the RRF region, based on both figures (Figure 4.15 and 4.16) again it can be proposed that the minimum recommended extension for the RRF can be RRF5. With this selection, numerical values of shear rate for this particular impeller will be accurate and well represented in both flow regimes.

4.4 RRF recommended extension

Based on the analysis developed in this chapter, a general conclusion can be drawn. By adopting extensions equal to that of RRF5 for both impellers (Figure 4.17), accurate and reliable numerical approximations will be obtained regardless of the flow regimen under consideration.

Figure 4.17 Stirred-tank systems embedded with the recommended extension for the RRF region for: a) four flat-blade turbine, b) Norstone® impeller

4.5 Case study: Experimental system previously reported

In order to test the results obatined in this research work concerning the recommended location for the surface separating the RRF and SRF regions for a stirred-tank equipped with the four flat-blade turbine conducting mixing operations at fully turbulent conditions, an additional CFD model of an experimental agitation system published by (Suzukawa, Kato, et al., 2006; Suzukawa, Mochizuki, et al., 2006) was reproduced. On these works, these authors conducted experiments considering several four flat-blade turbines with four different attack angles, 45°, 60°, 75° and 90°, respectively. Using Laser-Doppler velocimetry (LDV) techniques, they collected a set of readings for the mean velocity components corresponding to the impeller blade passage over an angle span of 90° between two neighboring baffles. For the purposes of this study, it was considered exclusively the data representing the 90° four flat-blade turbine. This selection lead to the desing of its corresponding computational mesh with the impeller blade located halfway along the arc between the baffles. The information corresponding to the experimental setup can be consulted in the references of (Suzukawa, Kato, et al., 2006; Suzukawa, Mochizuki, et al., 2006) and only relevant details in the context of this work are indicated below.

The system investigated was a flat bottom cylindrical stirred-tank equipped with four equally-spaced vertical baffles of width J = T/10, with no gap between the vessel wall and the baffles. These authors defined the ratios C/T=D/T=0.5, Z/T=1, D/W=5, with T=490 mm and W=24.5 mm. The working fluid considered was drinking water. The stirred-tank was operated at an impeller rotational speed of 2 rev/sec, leading to a tip velocity of 1.54 $m \cdot s^{-1}$ and $Re=1.2x10^5$, corresponding to fully turbulent conditions, thus allowing for the employment for the κ-ε model to account for turbulent effects.

The digital replica built based on the results obatined in the previous section is shown in Fig. 4.18, and as can be noticed, just two fluid volumes comprised the RRF, i.e., RRF=BSV+V1. It is worth to mention that the choice of the extension of the RRF for this mesh is equivalent to RRF5, i.e., a radial and height extensions of 1.54R and 1.47R (see Table 4.2).

In analogy to the replicas assembled in the previous section, a mesh independence analysis similar to that described in sections 3.3 was imposed on this computational mesh. The grid resolution study was conducted employing five conformal grids of different sizes, ranging from 808655 to 5384051 cells. It was found that a grid with 3530199 cells was the most adequate and was therefore used in the computations. This independent mesh consisted of 393046 elements in the BSV zone, 776102 elements in V1 and 2361051 in the SRF. For this independence analysis, all meshes generated showed a skewness not greater than 0.89. The numerical considerations employed for the simulations were the same as those described in section 3.2 for turbulent flow regime.

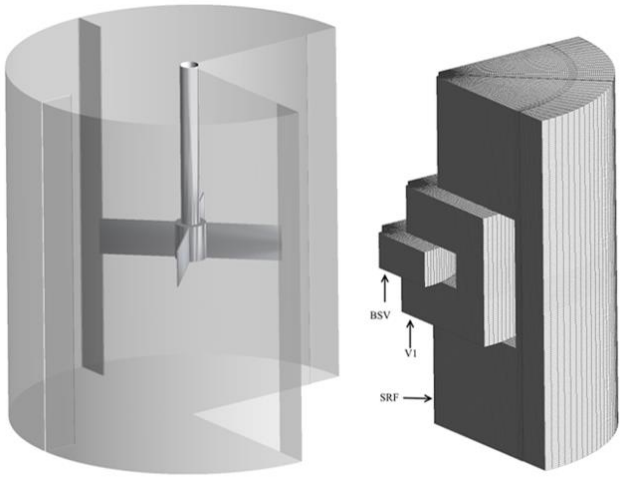

Figure 4.18 Computational mesh of the experimental system proposed by (Suzukawa, Kato, et al., 2006; Suzukawa, Mochizuki, et al., 2006).

In Table 4.3 the simulation results and the experimental data reported by (Suzukawa, Kato, et al., 2006; Suzukawa, Mochizuki, et al., 2006) are compared. These data consist of the dimensionless tangential velocity component (v_Θ) at the impeller mid-plane (y=0) at two dimensionless radial distances $x_1/R=0.49$ and $x_2/R=0.816$ when the impeller blade is located halfway between two immediate baffles (Suzukawa, Kato, et al., 2006). Also, the N_P and dimensionless values of the flow induced by the impeller $[Q/(v_{tip}R^2)]$ (Suzukawa, Mochizuki, et al., 2006) are compared. The flow induced by the impeller (Q) through an extra cylinder-like surface surrounding it was calculated according to (Suzukawa, Kato, et al., 2006):

$$Q = 4\left[2\pi\left(R+2.5\right)\right]\int_{y=-25\ mm}^{y=25\ mm} v_r\ dy. \tag{46}$$

The factor four in Eq. (46) was included to account for the system periodicity. As can be noticed in Table 4.3, there is reasonable agreement between simulation results and experimental measurements of the parameters N_P, $Q/(v_{tip}R^2)$ and dimensionless local tangential velocities evaluated in the blade-swept region. The reliable numerical results obtained for this real agitated system corroborate that the recommended dimensions employed for the RRF region, as well as the numerical considerations followed for CFD simulations, are adequate to predict the hydrodynamic evaluated parameters.

Table 4.3 Comparison between numerical predictions and reported experimental data, Re=1.2x10^5.

Parameter evaluated	Experimental from: (Suzukawa, Kato, et al., 2006; Suzukawa, Mochizuki, et al., 2006)	Numerical from this work	% error
N_P	4.72	4.08	13.6
$Q/v_{tip}R^2$	0.974	0.993	2
v_Θ/v_{tip}, x/R=0.49, y=0	0.41	0.43	4.9
v_Θ/v_{tip}, x/R=0.82, y=0	0.42	0.437	4.1

5 CONCLUSIONS

A CFD research work was conducted in order to evaluate the effect of modifying the location of the surface separating the RRF and SRF regions on numerical values of power number, shear rate and local velocity profiles. To this end, the MRF approach was employed to account for the rotation of the impeller-shaft array within numerical simulations of a baffled-tank embedded either with the four flat-blade turbine or the Norstone® impeller. The numerical study was carried out conducting mixing operations at laminar and turbulent flow conditions.

To account for varying the location of the separating surface, six different volumes comprising the rotating domain surrounding the impeller were defined in each of the digital replicas representing the baffled stirred-tank system. Numerical results show that for the lowest part of the laminar regime corresponding to creeping flow conditions (Re=4.9), no relevant discrepancies were detected on the numerical approximations retrieved from both digital replicas when variations in the location of the separating surface were imposed. However, as the Re increases (around Re=29.4), the extension of the RRF region begins to play a relevant role in the computations. According to the results obtained, the extension of the RRF domain depends on the flow regime, i.e., as the Re increases, the location of the separating surface has to be placed further away from the impeller surfaces considered in this work in order to enhance reliability of the numerical results.

An grid-density-based analysis for the two digital replicas built for this study, revealed that numerical power number values and local velocity profiles are more sensitive to changes in the extension of the RRF domain rather than to an increase in the number of grid points for the mesh representing the stirred-tank system equipped with the four flat-blade turbine. On the other hand, in the case of the digital replica representing the stirred-tank system equipped with the Norstone® impeller, sensitive changes were only substantial in the case of the velocity profiles.

It was found that in order to enhance reliability of the hydrodynamical parameters studied, a dimensionless radial extension corresponding to RRF5 has to be considered in both digital replicas, however, in the case of defining the recommended axial extent on which to place the surface separating the RRF and SRF regions, for the case of the four flat-blade turbine this has to be placed exactly at the location of RRF5, whereas for the Norstone® impeller this at first can be located as close to this impeller as is provided by RRF1, however, better and more accurate results can be obtained if this axial extension is enlarged to match that of RRF5. This phenomenon exhibited by the four flat-blade turbine on which the hydrodynamical parameters analyzed are sensitive to changes in the axial location of the separating surface, might be attributed to its capability to induce more pumping than the Norstone® impeller.

The applicability of this methodology was limited exclusively to impellers inducing a predominantly radial flow, this with the objective of evaluating the effect on the size of the RRF region within the MRF approach. To this end, two impellers possessing two different capacities of inducing pumping in the radial direction were considered. The dimensionless results exhibited in this research work were computed based on the impeller radius. The methodology presented was validated taking into account an experimental system previously reported in the scientific literature with dimensions bigger than those considered in this work, this result suggests that this methodology can be scale-up. However, the applicability of the methodology for large scale industrial tanks should be investigated and represents an open line of research.

Finally, further research works might bring light to actual knowledge by extending this methodology now considering other impeller types e.g., mixed (pitched blade) or axial (hydrofoils) flow impellers. However, numerical studies of these impellers should be addressed with more detail in future works.

Appendix A. ***The divergence theorem***.

This theorem states that for a continuous vector field $\vec{F}$ in a finite (bounded) closed region Ω, a transformation between a volume integral and an area integral can be established as follows:

$$\int_V \frac{d}{dx_i}\cdot\left(\vec{F}\right)dV = \int_A \overrightarrow{n_{x_i}}\cdot\left(\vec{F}\right)dA, \qquad \textbf{A1}$$

where $\overrightarrow{n_{x_i}}$ is a unitary vector parallel to the direction x_i but normal to the surface dA. An important consequence of the previous equation, is that it provides a way to compute the effects of the vector field $\vec{F}$ over the bounded region Ω by performing integration of the dot product $\overrightarrow{n_{x_i}}\cdot\left(\vec{F}\right)$, rather than finding and expression for the derivative $\frac{d}{dx_i}\cdot\left(\vec{F}\right)$. Although the divergence theorem considers performing a volume integral over the derivative $\frac{d}{dx_i}\cdot\left(\vec{F}\right)$, its convenience can be confirmed by noticing that in the case of a second derivative:

$$\frac{d^2}{dx_i^2}\left(\vec{F}\right) = \frac{d}{dx_i}\cdot\left[\frac{d}{dx}\left(\vec{F}\right)\right]. \qquad \textbf{A2}$$

application of equation **A1** over equation **A2** yields:

$$\int_V \frac{d^2}{dx_i^2}\left(\vec{F}\right)dV = \int_V \frac{d}{dx_i}\cdot\left[\frac{d}{dx}\left(\vec{F}\right)\right]dV = \int_A \overrightarrow{n_{x_i}}\cdot\left[\frac{d}{dx}\left(\vec{F}\right)\right]dA, \qquad \textbf{A3}$$

from equations **A2** and **A3**, it can be noticed that the transformation proposed by this theorem reduces from ***n*** to ***n-1*** the order of the derivative $\frac{d^n}{dx_i^n}$.

Appendix B. ***Taylor Series Expansion.***

Let $f:\mathbb{R}\to\mathbb{R}$ be a class *n+1* continuous function over the open interval $I=(x-\Delta x,x+\Delta x).$ Then for $x_1,x_2\in I$, $x_1\neq x_2$, exists a couple of numbers ξ_1 and ξ_2 such that:

$$f(x+\Delta x)=\sum_{k=0}^{n}\frac{f^{(k)}(x)(\Delta x)^k}{k!}+\frac{f^{(n+1)}(\xi_2)(\Delta x)^{n+1}}{(n+1)!}, \qquad \textbf{B1}$$
$$f(x-\Delta x)=\sum_{k=0}^{n}\frac{f^{(k)}(x)(-\Delta x)^k}{k!}+\frac{f^{(n+1)}(\xi_1)(-\Delta x)^{n+1}}{(n+1)!}.$$

For instance, for a class *n+1=3>2* function we have:

$$f(x+\Delta x)=\sum_{k=0}^{2}\frac{f^{(k)}(x)(\Delta x)^k}{k!}+\frac{f^{(3)}(\xi_2)(\Delta x)^3}{3!}, \qquad \textbf{B2}$$
$$f(x+\Delta x)=f(x)+f'(x)(\Delta x)+\frac{f''(x)(\Delta x)^2}{2}+\frac{f^{(3)}(\xi_2)(\Delta x)^3}{3!},$$

similarly, for the same function, its Taylor series expansion around the point $x-\Delta x$ is

$$f(x-\Delta x)=\sum_{k=0}^{2}\frac{f^{(k)}(x)(-\Delta x)^k}{k!}+\frac{f^{(3)}(\xi_1)(-\Delta x)^3}{3!}, \qquad \textbf{B3}$$
$$f(x-\Delta x)=f(x)-f'(x)(\Delta x)+\frac{f''(x)(\Delta x)^2}{2}+\frac{f^{(3)}(\xi_1)(-\Delta x)^3}{3!},$$

Performing the subtraction **B2**-**B3**

$$f(x+\Delta x)-f(x-\Delta x)=\underbrace{\left[f(x)-f(x)\right]}_{0}+\left[f'(x)(\Delta x)+f'(x)(\Delta x)\right]+\underbrace{\left[\frac{f''(x)(\Delta x)^2}{2}-\frac{f''(x)(\Delta x)^2}{2}\right]}_{0}$$

$$+\left[\frac{f^{(3)}(\xi_2)(\Delta x)^3}{3!}-\frac{f^{(3)}(\xi_1)(\Delta x)^3}{3!}\right],$$

$$f(x+\Delta x)-f(x-\Delta x)=\left[2f'(x)(\Delta x)\right]+\frac{(\Delta x)^3}{3!}\underbrace{\left[f^{(3)}(\xi_2)-f^{(3)}(\xi_1)\right]}_{G(\xi_1,\xi_2)},$$

from which we can obtain $f'(x)$:

$$f'(x)=\frac{f(x+\Delta x)-f(x-\Delta x)}{2\Delta x}-\frac{(\Delta x)^2}{2\cdot 3!}\cdot G(\xi_1,\xi_2),$$
$$f'(x)=\frac{f(x+\Delta x)-f(x-\Delta x)}{2\Delta x}+O(\Delta x)^2.$$

This proves that the error (order) of the estimator

$$f'(x)\cong\frac{f(x+\Delta x)-f(x-\Delta x)}{2\Delta x}, \qquad \textbf{B4}$$

Is $O(\Delta x)^2$.

Appendix C. ***Error order for the expression*** $(f(x+\Delta x)+f(x-\Delta x))/2$.

By adding **B2** and **B3**:

$$f(x+\Delta x)+f(x-\Delta x)=\left[f(x)+f(x)\right]+\underbrace{\left[f'(x)(\Delta x)-f'(x)(\Delta x)\right]}_{0}+\left[\frac{f''(x)(\Delta x)^2}{2}+\frac{f''(x)(\Delta x)^2}{2}\right]$$

$$+\left[\frac{f^{(3)}(\xi_1)(\Delta x)^3}{3!}-\frac{f^{(3)}(\xi_2)(\Delta x)^3}{3!}\right],$$

$$f(x+\Delta x)+f(x-\Delta x)=2f(x)+f''(x)(\Delta x)^2+\frac{(\Delta x)^3}{3!}\underbrace{\left[f^{(3)}(\xi_1)+f^{(3)}(\xi_2)\right]}_{G(\xi_1,\xi_2)},$$

some arrangements can be made

$$\frac{f(x+\Delta x)+f(x-\Delta x)}{2}=f(x)+\frac{f''(x)(\Delta x)^2}{2}+\frac{(\Delta x)^3}{2\cdot 3!}\underbrace{\left[f^{(3)}(\xi_1)+f^{(3)}(\xi_2)\right]}_{G(\xi_1,\xi_2)},$$

$$\frac{f(x+\Delta x)+f(x-\Delta x)}{2}-f(x)=\frac{f''(x)(\Delta x)^2}{2}+\frac{(\Delta x)^3}{2\cdot 3!}\cdot G(\xi_1,\xi_2)$$

Taking the absolute value of the previous equation

$$\left|\frac{f(x+\Delta x)+f(x-\Delta x)}{2}-f(x)\right|=\left|\frac{f''(x)(\Delta x)^2}{2}+\frac{(\Delta x)^3}{2\cdot 3!}\cdot G(\xi_1,\xi_2)\right|$$

$$\left|\frac{f(x+\Delta x)+f(x-\Delta x)}{2}-f(x)\right|\le\left|\frac{f''(x)(\Delta x)^2}{2}\right|+\left|\frac{(\Delta x)^3}{2\cdot 3!}\cdot G(\xi_1,\xi_2)\right|$$

$$\left|\frac{f(x+\Delta x)+f(x-\Delta x)}{2}-f(x)\right|\leq\left|\frac{f^{''}(x)}{2}\right|\cdot\left|(\Delta x)^2\right|+\left|\frac{G(\xi_1,\xi_2)}{2\cdot 3!}\right|\left|(\Delta x)^3\right| \qquad \textbf{C1}$$

Where it can be seen that the error for the expression in the left part of **C1** is determined by $(\Delta x)^2$.

Appendix D. **Second Order Polynomial Fitting.**

The problem here consists in finding coefficients $A,B,C\in\mathbb{R}$, such that for consecutive points x_1,x_2,x_3, the next system of second order polynomial equations holds:

$$\begin{aligned} f(x_1)&=f_1=Ax_1^2+Bx_1+C,\\ f(x_2)&=f_2=Ax_2^2+Bx_2+C,\\ f(x_3)&=f_3=Ax_3^2+Bx_3+C, \end{aligned} \qquad \textbf{D1}$$

which can be expressed in matrix form as follows:

$$\begin{bmatrix}1 & x_1 & x_1^2\\ 1 & x_2 & x_2^2\\ 1 & x_3 & x_3^2\end{bmatrix}\begin{bmatrix}C\\ B\\ A\end{bmatrix}=\begin{bmatrix}f_1\\ f_2\\ f_3\end{bmatrix}. \qquad \textbf{D2}$$

It turns out that the previous system has a solution according to:

$$\begin{bmatrix}C\\ B\\ A\end{bmatrix}=\begin{bmatrix}1 & x_1 & x_1^2\\ 1 & x_2 & x_2^2\\ 1 & x_3 & x_3^2\end{bmatrix}^{-1}\begin{bmatrix}f_1\\ f_2\\ f_3\end{bmatrix}, \qquad \textbf{D3}$$

where the elements of the inverse Vandermonde matrix are determined as:

$$\begin{bmatrix} 1 & x_1 & x_1^2 \\ 1 & x_2 & x_2^2 \\ 1 & x_3 & x_3^2 \end{bmatrix}^{-1} = \begin{bmatrix} V_{11}^{-1} & V_{12}^{-1} & V_{13}^{-1} \\ V_{21}^{-1} & V_{22}^{-1} & V_{23}^{-1} \\ V_{31}^{-1} & V_{32}^{-1} & V_{33}^{-1} \end{bmatrix}, \qquad \textbf{D4}$$

$$V_{11}^{-1} = \frac{x_2 x_3}{(x_2 - x_1)(x_3 - x_1)} \quad ; \quad V_{12}^{-1} = \frac{x_1 x_3}{(x_2 - x_1)(x_3 - x_2)} \quad ; \quad V_{13}^{-1} = \frac{x_1 x_2}{(x_3 - x_1)(x_3 - x_2)}$$
$$V_{21}^{-1} = \frac{-(x_2 + x_3)}{(x_2 - x_1)(x_3 - x_1)} \quad ; \quad V_{22}^{-1} = \frac{(x_1 + x_3)}{(x_2 - x_1)(x_3 - x_2)} \quad ; \quad V_{23}^{-1} = \frac{-(x_1 + x_2)}{(x_3 - x_1)(x_3 - x_2)}$$
$$V_{31}^{-1} = \frac{1}{(x_2 - x_1)(x_3 - x_1)} \quad ; \quad V_{32}^{-1} = \frac{-1}{(x_2 - x_1)(x_3 - x_2)} \quad ; \quad V_{33}^{-1} = \frac{1}{(x_3 - x_1)(x_3 - x_2)}$$

therefore, the coefficients $A, B, C,$ for the polynomial $f(x) = Ax^2 + Bx + C$ are determined by:

$$\begin{bmatrix} C \\ B \\ A \end{bmatrix} = \begin{bmatrix} V_{11}^{-1} & V_{12}^{-1} & V_{13}^{-1} \\ V_{21}^{-1} & V_{22}^{-1} & V_{23}^{-1} \\ V_{31}^{-1} & V_{32}^{-1} & V_{33}^{-1} \end{bmatrix} \begin{bmatrix} f_1 \\ f_2 \\ f_3 \end{bmatrix},$$

$$\begin{aligned} C &= (V_{11}^{-1} \cdot f_1) + (V_{12}^{-1} \cdot f_2) + (V_{13}^{-1} \cdot f_3), \\ B &= (V_{21}^{-1} \cdot f_1) + (V_{22}^{-1} \cdot f_2) + (V_{23}^{-1} \cdot f_3), \\ A &= (V_{31}^{-1} \cdot f_1) + (V_{32}^{-1} \cdot f_2) + (V_{33}^{-1} \cdot f_3). \end{aligned} \qquad \textbf{D5}$$

For instance, for an interior point x_{int} in between x_2 and x_3

$$\begin{aligned} f(x_{\text{int}}) &= f_{\text{int}} = Ax_{\text{int}}^2 + Bx_{\text{int}} + C, \\ f_{\text{int}} &= \left[(V_{31}^{-1} \cdot f_1) + (V_{32}^{-1} \cdot f_2) + (V_{33}^{-1} \cdot f_3) \right] x_{\text{int}}^2 \\ &+ \left[(V_{21}^{-1} \cdot f_1) + (V_{22}^{-1} \cdot f_2) + (V_{23}^{-1} \cdot f_3) \right] x_{\text{int}} \\ &+ \left[(V_{11}^{-1} \cdot f_1) + (V_{12}^{-1} \cdot f_2) + (V_{13}^{-1} \cdot f_3) \right], \end{aligned}$$

grouping in terms of f_1, f_2 and f_3

$$f_{\text{int}} = \underbrace{\left[(V_{31}^{-1}\cdot x_{\text{int}}^2)+(V_{21}^{-1}\cdot x_{\text{int}})+(V_{11}^{-1})\right]}_{\Phi_1} f_1$$
$$+\underbrace{\left[(V_{32}^{-1}\cdot x_{\text{int}}^2)+(V_{22}^{-1}\cdot x_{\text{int}})+(V_{12}^{-1})\right]}_{\Phi_2} f_2 \qquad \textbf{D6}$$
$$+\underbrace{\left[(V_{33}^{-1}\cdot x_{\text{int}}^2)+(V_{23}^{-1}\cdot x_{\text{int}})+(V_{13}^{-1})\right]}_{\Phi_3} f_3.$$

Equation D6 requires finding suitable expressions for Φ_1, Φ_2 and Φ_3. Considering the results from equation D4 then

$$\Phi_1 = \frac{x_{\text{int}}^2}{(x_2-x_1)(x_3-x_1)} + \frac{-x_{\text{int}}(x_2+x_3)}{(x_2-x_1)(x_3-x_1)} + \frac{x_2x_3}{(x_2-x_1)(x_3-x_1)},$$
$$\Phi_1 = \frac{x_{\text{int}}^2 - x_{\text{int}}(x_2+x_3)+x_2x_3}{(x_2-x_1)(x_3-x_1)},$$

If we suppose that x_{int} is located halfway between x_2 and x_3, i.e., $x_{\text{int}} = x_2 + \frac{(x_3-x_2)}{2} = \frac{x_3+x_2}{2}, \Rightarrow x_3+x_2 = 2x_{\text{int}}$, and in addition, if x_1, x_2, x_3 are equally spaced between them, i.e., $|x_3-x_2| = |x_2-x_1| = \Delta x, \Rightarrow |x_3-x_1| = 2\Delta x$, then, it can be proved that:

$$\Phi_1 = -\frac{1}{8}\ .$$

Similar arguments can be employed to find expressions for Φ_2 and Φ_3, but now noticing that there are two alternative ways to reach x_{int} either from x_2 or x_3, i.e., $x_{\text{int}} = x_2 + \Delta x/2$, or $x_{\text{int}} = x_3 - \Delta x/2$, so for Φ_2 and Φ_3

$$\Phi_2 = \frac{-x_{\text{int}}^2}{(x_2 - x_1)(x_3 - x_2)} + \frac{x_{\text{int}}(x_1 + x_3)}{(x_2 - x_1)(x_3 - x_2)} - \frac{x_1 x_3}{(x_2 - x_1)(x_3 - x_2)},$$

$$\Phi_2 = \frac{-x_{\text{int}}^2 + x_{\text{int}}(x_1 + x_3) - x_1 x_3}{(x_2 - x_1)(x_3 - x_2)},$$

$$\Phi_2 = \frac{6}{8},$$

$$\Phi_3 = \frac{x_{\text{int}}^2}{(x_3 - x_1)(x_3 - x_2)} + \frac{-x_{\text{int}}(x_1 + x_2)}{(x_3 - x_1)(x_3 - x_2)} - \frac{x_1 x_2}{(x_3 - x_1)(x_3 - x_2)},$$

$$\Phi_3 = \frac{x_{\text{int}}^2 - x_{\text{int}}(x_1 + x_2) + x_1 x_2}{(x_3 - x_1)(x_3 - x_2)},$$

$$\Phi_3 = \frac{3}{8},$$

So, finally

$$f_{\text{int}} = -\frac{1}{8} f_1 + \frac{6}{8} f_2 + \frac{3}{8} f_3. \qquad \textbf{D7}$$

In order to find out the error of the previous equation, let us consider a Taylor series around the points x_1, x_2, x_3 as follows:

$$f_1 = f(x_{\text{int}} - \frac{3}{2}\Delta x) = f_{\text{int}} - f_{\text{int}}^{'}(\frac{3\Delta x}{2}) + \frac{f_{\text{int}}^{''}}{2!}(\frac{3\Delta x}{2})^2 - \frac{f^{'''}(\xi_1)}{3!}(\frac{3\Delta x}{2})^3,$$

$$f_2 = f(x_{\text{int}} - \frac{\Delta x}{2}) = f_{\text{int}} - f_{\text{int}}^{'}(\frac{\Delta x}{2}) + \frac{f_{\text{int}}^{''}}{2!}(\frac{\Delta x}{2})^2 - \frac{f^{'''}(\xi_2)}{3!}(\frac{\Delta x}{2})^3,$$

$$f_3 = f(x_{\text{int}} + \frac{\Delta x}{2}) = f_{\text{int}} + f_{\text{int}}^{'}(\frac{\Delta x}{2}) + \frac{f_{\text{int}}^{''}}{2!}(\frac{\Delta x}{2})^2 + \frac{f^{'''}(\xi_3)}{3!}(\frac{\Delta x}{2})^3,$$

thus, according to (D7) the following sum can be computed:

$$-\frac{1}{8}\left[f_{\text{int}} - f_{\text{int}}^{'}(\frac{3\Delta x}{2}) + \frac{f_{\text{int}}^{''}}{2!}(\frac{3\Delta x}{2})^2 - \frac{f^{'''}(\xi_1)}{3!}(\frac{3\Delta x}{2})^3 \right] + \frac{6}{8}\left[f_{\text{int}} - f_{\text{int}}^{'}(\frac{\Delta x}{2}) + \frac{f_{\text{int}}^{''}}{2!}(\frac{\Delta x}{2})^2 - \frac{f^{'''}(\xi_2)}{3!}(\frac{\Delta x}{2})^3 \right]$$
$$+\frac{3}{8}\left[f_{\text{int}} + f_{\text{int}}^{'}(\frac{\Delta x}{2}) + \frac{f_{\text{int}}^{''}}{2!}(\frac{\Delta x}{2})^2 + \frac{f^{'''}(\xi_3)}{3!}(\frac{\Delta x}{2})^3 \right],$$

after a fair amount of algebra, it can be demonstrated that the previous expression has the form

$$\underbrace{\left[-\frac{1}{8}+\frac{6}{8}+\frac{3}{8}\right]}_{1} f_{\text{int}} + \underbrace{\left[\frac{3}{8}-\frac{6}{8}+\frac{3}{8}\right]}_{0} f_{\text{int}}^{'}\left(\frac{\Delta x}{2}\right)$$
$$+\underbrace{\left[(-\frac{1}{8}\cdot 3^2)+\frac{6}{8}+\frac{3}{8}\right]}_{0}\frac{f_{\text{int}}^{'}}{2!}\left(\frac{\Delta x}{2}\right)^2 + \left[O_1(\Delta x^3)+O_2(\Delta x^3)+O_3(\Delta x^3)\right],$$
$$= f_{\text{int}} + O(\Delta x^3). \qquad \textbf{D8}$$

Finally, from equation (D8) it can be seen that:

$$\left|\left(-\frac{1}{8}f_1+\frac{6}{8}f_2+\frac{3}{8}f_3\right)-f_{\text{int}}\right| \le \left|O(\Delta x^3)\right|, \qquad \textbf{D9}$$

which proves the error order of f_{int} to be $O(\Delta x^3)$. A natural question arising when employing equation (D7) points to the value of the derivative $f_{\text{int}}^{'}$. To address this issue, let us consider again $f(x) = Ax^2 + Bx + C$ and taking its derivative at the location x_{int}

$$f'_{\text{int}} = 2Ax_{\text{int}} + B,$$
$$f'_{\text{int}} = 2\left[V'_{31} f_1 + V'_{32} f_2 + V'_{33} f_3\right] x_{\text{int}} + \left[V'_{21} f_1 + V'_{22} f_2 + V'_{23} f_3\right],$$
$$f'_{\text{int}} = \left[2V'_{31} x_{\text{int}} + V'_{21}\right] f_1 + \left[2V'_{32} x_{\text{int}} + V'_{22}\right] f_2 + \left[2V'_{33} x_{\text{int}} + V'_{23}\right] f_3,$$

Noticing that $x_{\text{int}} = x_2 + \dfrac{\Delta x}{2}$

$$f'_{\text{int}} = \left[\underbrace{\frac{2x_{\text{int}} - (x_2 + x_3)}{(x_2 - x_1)(x_3 - x_1)}}_{0}\right] f_1 + \left[\underbrace{\frac{-2x_{\text{int}} + x_1 + x_3}{(x_2 - x_1)(x_3 - x_2)}}_{-\frac{1}{\Delta x}}\right] f_2 + \left[\underbrace{\frac{2x_{\text{int}} - x_1 - x_3}{(x_3 - x_1)(x_3 - x_2)}}_{\frac{1}{\Delta x}}\right] f_3,$$
$$f'_{\text{int}} = \frac{1}{\Delta x} f_3 - \frac{1}{\Delta x} f_2,$$
$$f'_{\text{int}} = \frac{f_3 - f_2}{\Delta x},$$

which previously was proved to have error order $O(\Delta x^2)$.

REFERENCES

Abujelala, M. T., & Lilley, D. G. (1984). LIMITATIONS AND EMPIRICAL EXTENSIONS OF THE k-ε MODEL AS APPLIED TO TURBULENT CONFINED SWIRLING FLOWS. *Chemical Engineering Communications, 31*(1-6), 223-236. doi: 10.1080/00986448408911152

Ameur, H., & Bouzit, M. (2012). Mixing in shear thinning fluids. *Brazilian Journal of Chemical Engineering, 29*, 349-358.

Ammar, M., Driss, Z., Chtourou, W., & Abid, M. S. (2012). Effect of the Tank Design on the Flow Pattern Generated with a Pitched Blade Turbine. *IJMEA, 2*(1), 12-19. doi: https://doi.org/10.5923/j.mechanics.20120201.03

Apostol, T. M. (2007). *Calculus, Volume I, One-variable Calculus, with an Introduction to Linear Algebra* (Vol. 1): John Wiley & Sons.

Armenante, P. M., Luo, C., Chou, C.-C., Fort, I., & Medek, J. (1997). Velocity profiles in a closed, unbaffled vessel: comparison between experimental LDV data and numerical CFD predictions. *Chemical Engineering Science, 52*(20), 3483-3492. doi: https://doi.org/10.1016/S0009-2509(97)00150-4

Bender, C., Brody, D., & Meister, B. (2002). *Inverse of a Vandermonde matrix*.

Boussinesq, J. (1877). *Essai sur la théorie des eaux courantes*: Impr. nationale.

Brucato, Alberto, Ciofalo, Michele, Grisafi, Franco, & Micale, Giorgio. (1998). Numerical prediction of flow fields in baffled stirred vessels: A comparison of alternative modelling approaches. *Chem. Eng. Sci., 53*(21), 3653-3684. doi: https://doi.org/10.1016/S0009-2509(98)00149-3

Chtourou, W., Ammar, M., Driss, Z., & Abid, M. S. (2014). CFD Prediction of the Turbulent Flow Generated in Stirred Square Tank by a Rushton Turbine. *Energy Power Eng., 6*(5), 6. doi: https://doi.org/10.4236/epe.2014.65010

Deen, N. G., Solberg, T., & Hjertager, B. H. (2002). Flow Generated by an Aerated Rushton Impeller: Two-phase PIV Experiments and Numerical Simulations. *Can. J. Chem. Eng., 80*(4), 1-15. doi: https://doi.org/10.1002/cjce.5450800406

Deglon, D. A., & Meyer, C. J. (2006). CFD modelling of stirred tanks: Numerical considerations. *Minerals Engineering, 19*(10), 1059-1068. doi: https://doi.org/10.1016/j.mineng.2006.04.001

Devi, T. T., Kumar, B., & Patel, A. K. (2015). Detached Eddy Simulation of Turbulent Flow in Stirred Tank Reactor. *Procedia Eng., 127*, 87-94. doi: https://doi.org/10.1016/j.proeng.2015.11.430

Dickey, D. S., & Fasano, J. B. (2004). How geometry & viscosity influence mixing: look at the flow patterns to help select the best mixer impeller. *Chemical Engineering, 111*(2), 42-47.

Dijkstra, Y. (2014). *Turbulence modelling in environmental flows. Improving the accuracy of the k-e model by a mathematical transformation.*, Delft University of Technology, The Netherlands.

Eggels, J., Unger, F., Weiss, M., Westerweel, J., Adrian, R., Friedrich, R., & Nieuwstadt, F. (1994). Fully developed turbulent pipe flow: a comparison between direct numerical simulation and experiment. *Journal of Fluid Mechanics, 268*, 175-210.

Ein-Mozaffari, F., & Upreti, S. R. (2009). Using ultrasonic Doppler velocimetry and CFD modeling to investigate the mixing of non-Newtonian fluids possessing yield stress.

Chemical Engineering Research and Design, 87(4), 515-523. doi: https://doi.org/10.1016/j.cherd.2008.12.020

Fathi Roudsari, S., Turcotte, G., Dhib, R., & Ein-Mozaffari, F. (2012). CFD modeling of the mixing of water in oil emulsions. *Comput. Chem. Eng., 45*, 124-136. doi: https://doi.org/10.1016/j.compchemeng.2012.06.013

Fluent, A. (2015). Theory guide. *Ansys Inc*.

Galindo, E., & Nienow, A. W. (1992). Mixing of Highly Viscous Simulated Xanthan Fermentation Broths with the Lightnin A-315 Impeller. *Biotechnol. Progr., 8*(3), 233-239. doi: https://doi.org/10.1021/bp00015a009

Glover, G. C., & Fitzpatrick, J. (2007). Modelling vortex formation in an unbaffled stirred tank reactors. *Chemical Engineering Journal, 127*(1-3), 11-22.

Jenne, M., & Reuss, M. (1999). A critical assessment on the use of k–ε turbulence models for simulation of the turbulent liquid flow induced by a Rushton-turbine in baffled stirred-tank reactors. *Chemical Engineering Science, 54*(17), 3921-3941. doi: https://doi.org/10.1016/S0009-2509(99)00093-7

Jing, H., Li, C., & Zhou, B. (2006). *A Hybrid Five-Point Finite Difference Scheme for Convection-Diffusion Equations*. Paper presented at the European Conference on Computational Fluid Dynamics, The Netherlands.

Joshi, J. B., Nere, N. K., Rane, C. V., Murthy, B. N., Mathpati, C. S., Patwardhan, A. W., & Ranade, V. V. (2011a). CFD simulation of stirred tanks: Comparison of turbulence models (Part II: Axial flow impellers, multiple impellers and multiphase dispersions). *The Canadian Journal of Chemical Engineering, 89*(4), 754-816. doi: 10.1002/cjce.20465

Joshi, J. B., Nere, N. K., Rane, C. V., Murthy, B. N., Mathpati, C. S., Patwardhan, A. W., & Ranade, V. V. (2011b). CFD simulation of stirred tanks: Comparison of turbulence models. Part I: Radial flow impellers. *The Canadian Journal of Chemical Engineering, 89*(1), 23-82. doi: 10.1002/cjce.20446

Joshi, J. B., Tabib, M. V., Deshpande, S. S., & Mathpati, C. S. (2009). Dynamics of Flow Structures and Transport Phenomena, 1. Experimental and Numerical Techniques for Identification and Energy Content of Flow Structures. *Industrial & Engineering Chemistry Research, 48*(17), 8244-8284. doi: 10.1021/ie8012506

Karimi, M. (2014). *CFD ANALYSIS OF SOLID-LIQUID-GAS INTERACTIONS IN FLOTATION VESSELS*. (PhD Thesis), Stellenbosch University.

Karimi, M., Akdogan, G., & Bradshaw, S. M. (2012). EFFECTS OF DIFFERENT MESH SCHEMES AND TURBULENCE MODELS IN CFD MODELLING OF STIRRED TANKS. *Physicochemical Problems of Mineral Processing, 48*(2).

Kelly, W., & Gigas, B. (2003). Using CFD to predict the behavior of power law fluids near axial-flow impellers operating in the transitional flow regime. *Chem. Eng. Sci., 58*(10), 2141-2152. doi: https://doi.org/10.1016/S0009-2509(03)00060-5

Lane, G. L., Schwarz, M. P., & Evans, G. M. (2000). Chapter 34 - Comparison of CFD Methods for Modelling of Stirred Tanks. In H. E. A. van den Akker & J. J. Derksen (Eds.), *10th European Conference on Mixing* (pp. 273-280). Amsterdam: Elsevier Science.

Launder, B. E., & Spalding, D. B. (1974). The numerical computation of turbulent flows. *Computer Methods in Applied Mechanics and Engineering, 3*(2), 269-289. doi: https://doi.org/10.1016/0045-7825(74)90029-2

Lee, K. C., & Yianneskis, M. (1994). The extent of periodicity of the flow in vessels stirred by Rushton impellers. *AIChE Symposium Series, 9*, 5-18.

Lee, M., & Moser, R. D. (2015). Direct numerical simulation of turbulent channel flow up to $\mathit {Re} _ {{\it\tau}}\approx 5200$. *Journal of Fluid Mechanics, 774*, 395-415.

Leonard, B. P. (1979). A stable and accurate convective modelling procedure based on quadratic upstream interpolation. *Computer Methods in Applied Mechanics and Engineering, 19*(1), 59-98. doi: https://doi.org/10.1016/0045-7825(79)90034-3

Luo, J. (1993). Full flow field computation of mixing in baffled stirred vessels. *Trans. I. Chem. E., 71*, 342-344.

Luo, J., & Gosman, A. (1994). *Prediction of impeller-induced flow in mixing vessels using multiple frames of reference*.

Macon, N., & Spitzbart, A. (1958). Inverses of Vandermonde Matrices. *The American Mathematical Monthly, 65*(2), 95-100. doi: 10.2307/2308881

Martínez-de Jesús, G., Ramírez-Muñoz, J., García-Cortés, D., & Cota, L. G. (2017). Computational Fluid Dynamics Study of Flow Induced by a Grooved High-Shear Impeller in an Unbaffled Tank. *Chemical Engineering & Technology, 41*(3), 580-589. doi: 10.1002/ceat.201700091

Montante, G., Lee, K. C., Brucato, A., & Yianneskis, M. (2001). Numerical simulations of the dependency of flow pattern on impeller clearance in stirred vessels. *Chemical Engineering Science, 56*(12), 3751-3770. doi: https://doi.org/10.1016/S0009-2509(01)00089-6

Murthy, B. N., & Joshi, J. B. (2008). Assessment of standard k–ε, RSM and LES turbulence models in a baffled stirred vessel agitated by various impeller designs. *Chem. Eng. Sci., 63*(22), 5468-5495. doi: https://doi.org/10.1016/j.ces.2008.06.019

Murthy, J. Y., Mathur, S. R., & Choudhury, C. (1994). CFD simulation of flow in stirred tanks reactor using a sliding mesh technique. *Eighth European Conference on Mixing, 136*, 341-345.

Oshinowo, L., Jaworski, Z., Dyster, K. N., Marshall, E., & Nienow, A. W. (2000). Chapter 35 - Predicting the tangential velocity field in stirred tanks using the Multiple Reference Frames (MRF) model with validation by LDA measurements. In H. E. A. van den Akker & J. J. Derksen (Eds.), *10th European Conference on Mixing* (pp. 281-288). Amsterdam: Elsevier Science.

Pakzad, L., Ein-Mozaffari, F., & Chan, P. (2008). Using electrical resistance tomography and computational fluid dynamics modeling to study the formation of cavern in the mixing of pseudoplastic fluids possessing yield stress. *Chemical Engineering Science, 63*(9), 2508-2522. doi: https://doi.org/10.1016/j.ces.2008.02.009

Pakzad, L., Ein-Mozaffari, F., Upreti, S. R., & Lohi, A. (2013). Characterisation of the mixing of non-newtonian fluids with a scaba 6SRGT impeller through ert and CFD. *The Canadian Journal of Chemical Engineering, 91*(1), 90-100. doi: 10.1002/cjce.21616

Patil, H., Patel, A. K., Pant, H. J., & Venu Vinod, A. (2018). CFD simulation model for mixing tank using multiple reference frame (MRF) impeller rotation. *ISH Journal of Hydraulic Engineering*, 1-10.

Patton, T. C. (1979). *Paint Flow and Pigment Dispersion* (2 ed.). New York: Wiley Interscience Publishers.

Paul, E. L., Atiemo-Obeng, V. A., & Kresta, S. M. (2004). *Handbook of industrial mixing: science and practice*: John Wiley & Sons.

Perry, R. H., & Green, D. W. (2008). *Perry's chemical engineers' handbook*. New York: McGraw-Hill.

Pope, S. B. (2000). *Turbulent Flows*: Cambridge University Press.

Protter, M. H., & Morrey, C. B. J. (1997). *A First Course in Real Analysis*: Springer New York.

Rahimi, M., Kakekhani, A., & Alsairafi, A. A. (2010). Experimental and computational fluid dynamic (CFD) studies on mixing characteristics of a modified helical ribbon impeller. *Korean Journal of Chemical Engineering, 27*(4), 1150-1158. doi: 10.1007/s11814-010-0222-7

Ramírez-Gómez, R., García-Cortés, D., Martínez-de Jesús, G., González-Brambila, M. M., Alonso, A., Martínez-Delgadillo, S. A., & Ramírez-Muñoz, J. (2015). Performance Evaluation of Two High-Shear Impellers in an Unbaffled Stirred Tank. *Chemical Engineering & Technology, 38*(9), 1519-1529. doi: doi:10.1002/ceat.201400792

Ramírez-Muñoz, J., Guadarrama-Pérez, R., & Márquez-Baños, V. E. (2017). A direct calculation method of the Metzner-Otto constant by using computational fluid dynamics. *Chem. Eng. Sci., 174*, 347-353. doi: https://doi.org/10.1016/j.ces.2017.09.023

Ramírez-Muñoz, J., Martínez-de-Jesús, G., Soria, A., Alonso, A., & Torres, L. G. (2016). Assessment of the effective viscous dissipation for deagglomeration processes induced by a high shear impeller in a stirred tank. *Advanced Powder Technology, 27*(5), 1885-1897. doi: https://doi.org/10.1016/j.apt.2016.06.019

Rushton, J., & Oldshue, J. (1953). Mixing present theory and practice. *Chem. Eng. Prog., 49*, 161-168.

Scott-Pomerantz, C. D. (2005). *The k-epsilon model in the theory of turbulence*. (Doctoral Dissertation), University of Pittsburgh. Retrieved from http://d-scholarship.pitt.edu/10241/

Schlatter, P., & Örlü, R. (2010). Assessment of direct numerical simulation data of turbulent boundary layers. *Journal of Fluid Mechanics, 659*, 116-126.

Sommerfeld, M., & Decker, S. (2004). State of the Art and Future Trends in CFD Simulation of Stirred Vessel Hydrodynamics. *Chemical Engineering & Technology, 27*(3), 215-224. doi: 10.1002/ceat.200402007

Sossa-Echeverria, J., & Taghipour, F. (2012). Correction for "Mixing of Newtonian and Non-Newtonian Fluids in a Cylindrical Mixer Equipped with a Side-Entry Impeller". *Industrial & Engineering Chemistry Research, 51*(51), 16763-16763. doi: 10.1021/ie3032845

Speziale, C. G. (1991). Analytical methods for the development of Reynolds-stress closures in turbulence. *Annual Review of Fluid Mechanics, 23*(1), 107-157.

Spiegel, M. R. (1959). *Schaum's outline of theory and problems of vector analysis and an introduction to tensor analysis*: McGraw-Hill.

Spitzbart, A., & Macon, N. (1957). Numerical Differentiation Formulas. *The American Mathematical Monthly, 64*(10), 721-723. doi: 10.2307/2309751

Spivak, M. (1980). Calculus. Houston, TX: Publish or Perish: Inc.

Spivak, M. (2018). *Calculus on manifolds: a modern approach to classical theorems of advanced calculus*: CRC Press.

Suzukawa, K., Kato, K., Mochizuki, S., & Osaka, H. (2006). Vortex Structures around a Flat Paddle Impeller in a Stirred Vessel. *JSME International Journal Series B Fluids and Thermal Engineering*, *49*(2), 426-433. doi: 10.1299/jsmeb.49.426

Suzukawa, K., Mochizuki, S., & Osaka, H. (2006). Effect of the attack angle on the roll and trailing vortex structures in an agitated vessel with a paddle impeller. *Chem. Eng. Sci.*, *61*(9), 2791-2798. doi: https://doi.org/10.1016/j.ces.2005.10.063

Tabor, G., Gosman, A., & Issa, R. (1996). *Numerical simulation of the flow in a mixing vessel stirred by a Rushton turbine*. Paper presented at the Institution of Chemical Engineers Symposium Series.

Tamburini, A., Gagliano, G., Micale, G., Brucato, A., Scargiali, F., & Ciofalo, M. (2018). Direct numerical simulations of creeping to early turbulent flow in unbaffled and baffled stirred tanks. *Chemical Engineering Science, 192*, 161-175. doi: https://doi.org/10.1016/j.ces.2018.07.023

Turner, L. R. (1966). Inverse of the Vandermonde matrix with applications.

Versteeg, H. K., & Malalasekera, W. (2007). *An Introduction to Computational Fluid Dynamics: The Finite Volume Method*: Pearson Education Limited.

Wechsler, K., Breuer, M., & Durst, F. (1999). Steady and Unsteady Computations of Turbulent Flows Induced by a 4/45° Pitched-Blade Impeller. *J. Fluids Eng., 121*(2), 318-329. doi: https://doi.org/10.1115/1.2822210

Wu, H., & Patterson, G. K. (1989). Laser-Doppler measurements of turbulent-flow parameters in a stirred mixer. *Chemical Engineering Science, 44*(10), 2207-2221. doi: https://doi.org/10.1016/0009-2509(89)85155-3

Zadravec, M., Basic, S., & Hribersek, M. (2007). The influence of rotating domain size in a rotating frame of reference approach for simulation of rotating impeller in a mixing vessel. *J. Eng. Sci. Technol*, *2*(2), 126-138.

Zalc, J. M., Alvarez, M. M., Muzzio, F. J., & Arik, B. E. (2001). Extensive validation of computed laminar flow in a stirred tank with three Rushton turbines. *AIChE J.*, *47*(10), 2144-2154. doi: doi:10.1002/aic.690471003.